

Lab - Mechatronics
Modelling and control of a Magnetic Levitation System

Tommaso Bocchietti 10740309

Daniele Cianca 10764733

Sara Orazzo 10995845

A.Y. 2024/25



POLITECNICO
MILANO 1863

Contents

1	Introduction	4
2	Magnetic Levitation System	5
3	Modelling	7
3.1	Mathematical model	7
3.1.1	Lagrangian formulation	7
3.1.2	Electrical components model	8
3.1.3	Equations of motion	8
3.1.4	Model reduction	9
3.1.5	Control input correction	9
3.2	Model Linearization	10
3.2.1	Operating point computation	10
3.2.2	Linearized model derivation	10
3.3	State Space Representation	11
3.4	Single Coil Configuration	12
4	Identification	14
4.1	Direct measurement	14
4.2	Sensors characterization	14
4.2.1	Voltage to position mapping	14
4.2.2	Sensors noise analysis	15
4.3	Control to voltage	16
4.4	Inductances characterization	17
4.5	Force analysis	19
4.6	Active levitation (parameters validation)	21
5	Model Analysis	23
5.1	Controllability and observability	23
5.2	Open loop stability	23
5.3	Levitation region	25
6	Filters & Estimators Design	26
6.1	Low Pass Filter	26
6.2	Luenberger Observer	26
6.3	Kalman Filter	27
6.4	Extended Kalman Filter	28
7	Controllers Design	29
7.1	PID Controllers	29
7.1.1	PID classical	29
7.1.2	PID with Anti-Windup correction	30
7.1.3	PID with gain scheduling	31
7.2	LQ Controllers	32
7.2.1	LQR	33
7.2.2	LQR with tracking capabilities	33
7.2.3	LQI	35
7.3	MPC Controllers	36
8	Results	38
8.1	Controllers comparison	38
8.1.1	Multi-steps reference	38
8.1.2	Sinusoidal (discrete) reference	41
8.1.3	Conclusions	42
8.2	Filters and Estimators comparison	43
8.2.1	Conclusions	44
9	Conclusions	45

List of Figures

1	Magnetic Levitation System.	5
2	A schematic representation of MLS is shown. One might also appreciate the feedback loop that is closed by the optical sensor. Credit to [3].	5
3	Applications of Magnetic Levitation. Japan's MagLev train Chūō Shinkansen [6] on the left, independent 3D control of a pair of microrobots via MLS techniques [4] on the right.	6
4	Schematic representation of the MLS system and description of its components.	7
5	Position of the ball as a function of the output voltage of the infrared optical sensor.	15
6	Sensors' noise analysis.	15
7	Control to voltage identification	16
8	Inductance characterization for different currents and ball positions	18
9	Inductance model fitting	18
10	Position of the ball and current in the first coil around the levitation point (marked by vertical black dashed line)	20
11	Dynamic inductance characteristics and electromagnet force	20
12	Comparison of the operating point between the theoretical model and the experimental data obtained during the active levitation test.	21
13	Root Locus plot of the open loop system with direct and inverse proportional control.	24
14	Bode plot of the open loop system.	24
15	Levitation Region	25
16	Bode Plot, Root Locus and Step Response (PID classic)	30
17	Step Response (PID anti-windup)	31
18	Bode plot, Root Locus and Step Response (PID gain scheduling)	32
19	Step Response (PID gain scheduling)	32
20	Step Response	34
21	Step Response	36
22	Step Response (MPC)	37
23	Comparison of controllers with multistep stairs reference using KF	38
24	Comparison of controllers with multistep up & down reference using KF	39
25	PIDs, LQs, MPC with multistep up reference using KF	39
26	PIDs, LQs, MPC with multistep up & down (down) reference using KF	40
27	Comparison of controllers with sinusoidal fast reference using KF	41
28	PIDs, LQs, MPC with sinusoidal fast reference using KF	42
29	Comparison of filter using an LQR tracking with sinusoidal slow reference	43
30	Comparison of no filter, low pass, KF using an LQR tracking with sinusoidal slow reference	44

List of Tables

1	Directly measured parameters and constants	14
2	Standard deviation and covariance of the sensors' noise.	16
3	Control to voltage identification parameters	17
4	Inductance characterization parameters	19
5	Final inductance parameters obtained via active levitation test.	22
6	PID controller gains	31
7	Constraints for the MPC controller	37

1 Introduction

This laboratory experience focuses on the precise control of the levitation of a ferromagnetic object within a magnetic field, a setup commonly known as a Magnetic Levitation System (MLS). The MLS represents a fascinating and challenging application of control theory, involving highly nonlinear dynamics and unstable equilibrium conditions.

The project has been structured into two main phases:

- **System modelling and identification:** in this phase, the system has been modelled by means of both differential equations and state space representation, and the parameters of the model have been identified through experimental data performed directly on the real system. Some preliminary consideration about stability and controllability has also been made.
- **Filters, estimators and controllers design:** in this phase, many control techniques have been implemented and tested. The main goal was to compare the performances of different controllers in terms of stability, robustness and tracking capabilities.

Report structure This report covers all the aspects of the laboratory experience, from the theoretical background to the practical implementation of the control algorithms. In particular, in Section 2 a brief introduction to the MLS is given, along with some high-level overview of the physical phenomena involved. In Section 3 the model of the system is derived, while in Section 4 the parameters of the model are identified through experimental data or collected from the datasheet. Section 5 is dedicated to the analysis of the model, focusing on stability and controllability. In Section 6 some filters and estimators are designed to reduce noise and improve the performances of the controllers designed in Section 7. Finally, results are shown in Section 8 while in Section 9 some conclusions about the work done and possible future developments are drawn.

Tools An extensive use of **MATLAB** and **Simulink** has been made to implement the controllers and to simulate the system.

2 Magnetic Levitation System

As stated in the introduction, the system under study is the Magnetic Levitation System (MLS) provided by Inteco [2]. In Figure 1 the system used in this work is shown.

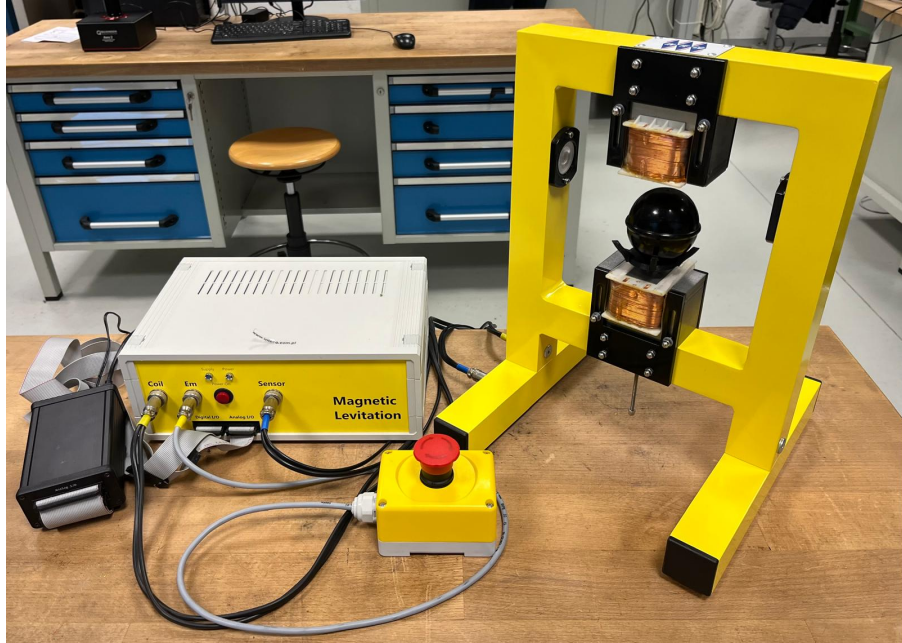


Figure 1: Magnetic Levitation System.

As it can be seen quite clearly, the system is composed of a simple mechanical structure that is used to support two electromagnets and an optical infrared sensor. Along with the mechanical structure, a ferromagnetic ball and a control unit are present. From the producer manual, the control unit is composed of a RTDAC/PCI I/O board with XILINX chip running at $40MHz$.

At its core principle, the system uses the interaction between the magnetic field generated by the electromagnets and the ferromagnetic ball to keep the ball in a desired position. The optical sensor is used to measure the position of the ball and provide feedback to the control unit that, in turn, adjusts the voltage applied to (and indeed the current flowing through) the electromagnets to keep the ball in a desired position. In Figure 2 a schematic representation of the upper half of the system is shown.

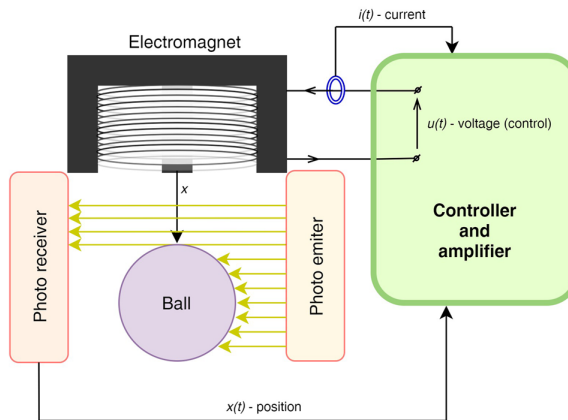


Figure 2: A schematic representation of MLS is shown. One might also appreciate the feedback loop that is closed by the optical sensor. Credit to [3].

Real world application Magnetic levitation systems have diverse and transformative applications across various industries.

One of the most prominent uses is in high-speed transportation, such as MagLev trains, which achieve speeds exceeding $500km/h$ by eliminating wheel-rail friction. These systems offer smoother rides, reduced noise, and lower

maintenance costs compared to traditional trains. Notable implementations include Japan's Chūō Shinkansen (see Figure 3a), aiming to connect Tokyo and Osaka, and China's 600km/h MagLev project, which demonstrates cutting-edge levitation control technology [6].

Other applications include microrobotics research, where magnetic levitation enables precise control of miniature robots for possible medical and industrial applications [7]. These robots can navigate complex environments, perform delicate tasks, and deliver targeted therapies with high precision and minimal invasiveness. Researchers are also exploring complex magnetic levitation environments for concurrent control of multiple robots, which could revolutionize microscale manufacturing and healthcare [4].

Additionally, scientific research benefits from these systems in experiments requiring vibration-free environments, such as advanced spectroscopy [1] and microgravity simulation [5].

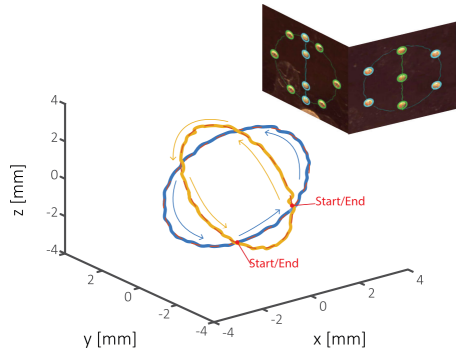


Figure 3: Applications of Magnetic Levitation. Japan's MagLev train Chūō Shinkansen [6] on the left, independent 3D control of a pair of microrobots via MLS techniques [4] on the right.

3 Modelling

The MLS is a complex system that can be divided into:

- **Electromagnetic subsystem:** it takes into account all the electrical components going from the power supply to the electromagnets themselves, and so the generation of the magnetic field by the coils;
- **Mechanical subsystem:** it takes into account the dynamics of the ball and the forces acting on it, including the electromagnetic forces generated by the magnetic field.

Due to the presence of the ball that moves inside a magnetic field, a complex connection between the two subsystems that goes beyond the simple force balance exists. For this reason, it's almost impossible to derive a complete model without considering both subsystems at the same time.

In Figure 4, a schematic representation of all the components of the system and the forces acting on it is shown. Instead, in Table 4 a brief description of the components is provided.

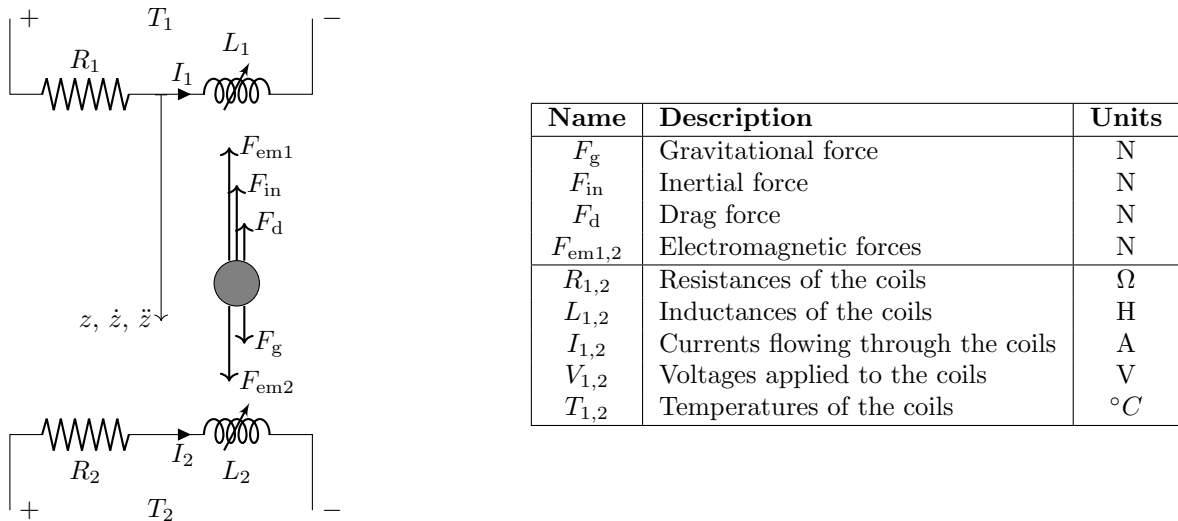


Figure 4: Schematic representation of the MLS system and description of its components.

In the following sections, we will derive the equations that governs the MLS system, adopting an energetic approach that starts from the energy conservation principle.

3.1 Mathematical model

We can now proceed with the derivation of the equations that govern the system.

At first, we can recall the energy conservation principle stating that the sum of the kinetic, potential, and dissipated energy of the system is equivalent to the work done by the external forces acting on it.

3.1.1 Lagrangian formulation

Thanks to Lagrange's equation we encapsulate the energy conservation principle by writing the following:

$$\frac{d}{dt} \left(\frac{\partial \mathcal{T}}{\partial \dot{\mathbf{u}}} \right) - \frac{\partial \mathcal{T}}{\partial \mathbf{u}} + \frac{\partial \mathcal{D}}{\partial \dot{\mathbf{u}}} + \frac{\partial \mathcal{U}}{\partial \mathbf{u}} = \mathcal{Q} \quad (1)$$

Where \mathbf{u} is the generalized coordinates of the system, \mathcal{T} is the kinetic energy, \mathcal{D} is the dissipated one, \mathcal{U} is the potential energy, and \mathcal{Q} is the generalized input to the system.

At first, we can give a definition of all the energetic terms included in Equation 1 for the MLS system. Notice that with respect to traditional purely mechanical systems, we also have to consider the stored energy in the coils as inductors, the dissipation due to the resistance of the coils, and the potential energy given by the external power supply.

By doing so, we can write the kinetic energy of the system as:

$$\mathcal{T} = \frac{1}{2} m \ddot{z}^2 + \frac{1}{2} L_1(z, \dot{q}_1, T_1) \dot{q}_1^2 + \frac{1}{2} L_2(z, \dot{q}_2, T_2) \dot{q}_2^2 \quad (2)$$

Where m is the mass of the ball, L_1 and L_2 are the inductances of the coils, and q_1 and q_2 are the charges stored in the coils. It follows that \dot{q}_1 and \dot{q}_2 are the currents flowing through the coils.

The dissipated energy of the system can be written as:

$$\mathcal{D} = \int_{\dot{z}(\cdot)} \frac{1}{2} C_d A \rho \dot{z}^2 d\dot{z} + \int_{q_1(\cdot)} R_1(\dot{q}_1, T_1) \dot{q}_1 dq_1 + \int_{q_2(\cdot)} R_2(\dot{q}_2, T_2) \dot{q}_2 dq_2 \quad (3)$$

Where C_d is the drag coefficient for a generic spherical object, A is the cross-sectional area of the ball, and ρ is the density of air.

Instead, the potential energy of the system can be written as:

$$\mathcal{U} = -mgz - q_1 V_1 - q_2 V_2 \quad (4)$$

Where V_1 and V_2 are the voltages applied to the coils.

Finally, the generalized input to the system can be evaluated as:

$$\mathcal{Q} = 0 \quad (5)$$

For convenience, we have chosen to consider both the external power supplied and the gravitational force as potential energy terms and not as generalized inputs. Notice also the minus sign in the gravitational potential energy term, which is due to the fact that the gravitational force tends to increase the potential energy with respect to the chosen reference frame (positive downwards, see Figure 4).

3.1.2 Electrical components model

Before proceeding, it's necessary to explicitly state the dependence of the inductance and resistance terms on the generalized coordinates of the system.

We can assume that, in first approximation, the sensitivity of both the electrical components to the temperature of the coils is negligible. This is strong and possibly incorrect assumption, but it allows us to simplify the model and focus on the main dynamics of the system.

Resistance model For what regards the resistance terms, we can assume that the resistance of the coils is constant and so does not depend on neither the current flowing through them nor the temperature of the coils. Under these assumptions, we can write the resistance terms as:

$$\begin{aligned} R_1 &= R_1(\dot{q}_1, T_1) = R_{10} \\ R_2 &= R_2(\dot{q}_2, T_2) = R_{20} \end{aligned} \quad (6)$$

Where R_{*0} are the resistances of the coils measured at ambient temperature with negligible current flowing through them.

Inductance model Considering the inductance terms, we will again neglect the dependence on the coil's temperature, but we will take into account the variation of the inductance due to the presence of the ball in the magnetic field (principal source of nonlinearity in the system) and also the dependence over the current flowing through the coils. For the assumption stated above, we will model the inductance terms as:

$$\begin{aligned} L_1 &= L_1(z, \dot{q}_1, T_1) = L_{10} + L_{1z} e^{-a_{1z} z} + L_{1I} * \arctan(a_{1I} I_1 - b_{1I}) \\ L_2 &= L_2(z, \dot{q}_2, T_2) = L_{20} + L_{2z} e^{-a_{2z}(h-2r-z)} + L_{2I} * \arctan(a_{2I} I_2 - b_{2I}) \end{aligned} \quad (7)$$

Where L_{*0} are the nominal inductances values. Instead, L_{*z} , a_{*z} and L_{*I} , a_{*I} , b_{*I} are coefficients that take into account the variation of the inductance due to the presence of the ball in the magnetic field and the current flowing through the coils, respectively.

It has to be noted that this model was suggested by a careful analysis of experimental data and is not directly based on theoretical considerations. Some previous models of inductance can also be found in the literature, but they are often too complex and not suitable for control purposes.

3.1.3 Equations of motion

Considering the assumptions made in both the resistance and inductance models (Equations 6, 7) to neglect their dependence on the temperature of the coils, we can see that the generalized coordinates are z , q_1 , and q_2 , and so the vector of generalized coordinates is $\mathbf{u} = [z, q_1, q_2]^T$.

Once \mathbf{u} has been identified, the procedure to derive the equations of motion is straightforward. Based on Equation 1, we can write the following system of equations:

$$\begin{cases} \frac{d}{dt} \left(\frac{\partial \mathcal{T}}{\partial \dot{z}} \right) - \frac{\partial \mathcal{T}}{\partial z} + \frac{\partial \mathcal{D}}{\partial \dot{z}} + \frac{\partial \mathcal{U}}{\partial z} = \mathcal{Q} \\ \frac{d}{dt} \left(\frac{\partial \mathcal{T}}{\partial \dot{q}_1} \right) - \frac{\partial \mathcal{T}}{\partial q_1} + \frac{\partial \mathcal{D}}{\partial \dot{q}_1} + \frac{\partial \mathcal{U}}{\partial q_1} = \mathcal{Q} \\ \frac{d}{dt} \left(\frac{\partial \mathcal{T}}{\partial \dot{q}_2} \right) - \frac{\partial \mathcal{T}}{\partial q_2} + \frac{\partial \mathcal{D}}{\partial \dot{q}_2} + \frac{\partial \mathcal{U}}{\partial q_2} = \mathcal{Q} \end{cases} \quad (8)$$

By substituting the energetic terms obtained in Equations 2, 3, 4, 5 into the set of equations above, we obtain the following equations of motion:

$$\begin{cases} m\ddot{z} - \frac{1}{2} \frac{\partial L_1}{\partial z} \dot{q}_1^2 - \frac{1}{2} \frac{\partial L_2}{\partial z} \dot{q}_2^2 + \frac{1}{2} C_d A \rho \dot{z} |\dot{z}| - mg = 0 \\ \frac{1}{2} \left(\frac{\partial^2 L_1}{\partial q_1 \partial z} \dot{z} + \frac{\partial^2 L_1}{\partial q_1^2} \ddot{q}_1 \right) \dot{q}_1^2 + \frac{\partial L_1}{\partial q_1} \dot{q}_1 \ddot{q}_1 + \left(\frac{\partial L_1}{\partial z} \dot{z} + \frac{\partial L_1}{\partial q_1} \ddot{q}_1 \right) \dot{q}_1 + L_1 \ddot{q}_1 + R_1 q_1 - V_1 = 0 \\ \frac{1}{2} \left(\frac{\partial^2 L_2}{\partial q_2 \partial z} \dot{z} + \frac{\partial^2 L_2}{\partial q_2^2} \ddot{q}_2 \right) \dot{q}_2^2 + \frac{\partial L_2}{\partial q_2} \dot{q}_2 \ddot{q}_2 + \left(\frac{\partial L_2}{\partial z} \dot{z} + \frac{\partial L_2}{\partial q_2} \ddot{q}_2 \right) \dot{q}_2 + L_2 \ddot{q}_2 + R_2 q_2 - V_2 = 0 \end{cases} \quad (9)$$

For convenience, we can replace time derivatives of charges leveraging the definition of current as the time derivative of the charge. Moreover, we can group the terms in the equations above so to move derivatives with respect to the generalized coordinates on the left-hand side of the equations. Finally, we also transform the second order differential equations into first order differential equations by introducing a fourth equation and considering the ball velocity v as a state variable. By doing so, we obtain the following set of equations:

$$\begin{cases} \dot{z} = v \\ \dot{v} = m^{-1} \left(\frac{1}{2} \frac{\partial L_1}{\partial z} I_1^2 + \frac{1}{2} \frac{\partial L_2}{\partial z} I_2^2 - \frac{1}{2} C_d A \rho \dot{z} |\dot{z}| + mg \right) \\ \dot{I}_1 = \left(\frac{1}{2} \frac{\partial^2 L_1}{\partial I_1^2} I_1^2 + 2 \frac{\partial L_1}{\partial I_1} I_1 + L_1 \right)^{-1} \left(-\frac{1}{2} \frac{\partial^2 L_1}{\partial I_1 \partial z} \dot{z} I_1^2 - \frac{\partial L_1}{\partial z} \dot{z} I_1 - R_1 I_1 + V_1 \right) = 0 \\ \dot{I}_2 = \left(\frac{1}{2} \frac{\partial^2 L_2}{\partial I_2^2} I_2^2 + 2 \frac{\partial L_2}{\partial I_2} I_2 + L_2 \right)^{-1} \left(-\frac{1}{2} \frac{\partial^2 L_2}{\partial I_2 \partial z} \dot{z} I_2^2 - \frac{\partial L_2}{\partial z} \dot{z} I_2 - R_2 I_2 + V_2 \right) = 0 \end{cases} \quad (10)$$

The set of equations above represents the complete mathematical model of the MLS system.

3.1.4 Model reduction

In order to simplify the model and make it more suitable for control purposes, we can make some assumptions that allow us to reduce the complexity of the system without losing its main dynamics.

Based also on the experimental data collected during the parameters' identification phase (Section 4), we can state that the sensitivity of the inductance terms to the current flowing through the coils is negligible around the operating point. Moreover, also the velocity of the ball will always be small, and so every term that is linearly dependent on it can be neglected. Based on these assumptions, we can impose the following conditions to the system:

$$\begin{cases} \frac{\partial L_*}{\partial I_*} \approx 0 \\ \frac{\partial^2 L_*}{\partial I_*^2} \approx 0 \\ \dot{z} \approx 0 \end{cases} \quad (11)$$

Equations of motion 10 consequently simplify to:

$$\begin{cases} \dot{z} = v \\ \dot{v} = m^{-1} \left(\frac{1}{2} \frac{\partial L_1}{\partial z} I_1^2 + \frac{1}{2} \frac{\partial L_2}{\partial z} I_2^2 + mg \right) \\ \dot{I}_1 = L_1^{-1} (-R_1 I_1 + V_1) \\ \dot{I}_2 = L_2^{-1} (-R_2 I_2 + V_2) \end{cases} \quad (12)$$

3.1.5 Control input correction

A final important remark has to be made about the input given to the system.

So far, in all the equations above, we have considered the input to the system as the voltage applied to the coils. However, the actual input to the system is the duty cycle of the PWM¹ signal that drives the coils.

Ideally, the relationship between the duty cycle and the voltage applied to the coils is a direct proportionality, but in practice, a linear approximation must be made. One can easily see that by simply connecting the power supply to the coils, a minimum voltage will be applied and a certain amount of current will flow through. In the following, we will refer to this current and voltage as I_{*min} and V_{*min} respectively. In the context of control purposes, these zones where it's not possible to have a direct control over the applied voltage are called *black zones*.

¹Pulse-Width Modulation

Under these considerations, one can rewrite the voltages applied to the coils V_* as a function of the duty cycle U_* as a piece wise linear function:

$$V_* = \begin{cases} k_* U_* + c_* & \text{if } U_* \geq U_{*min} \\ V_{*min} & \text{if } U_* < U_{*min} \end{cases} \quad (13)$$

Where k_* and c_* are the slope and the intercept of the linear relation, respectively, and U_{*min} is the minimum duty cycle that allows to move outside the black zone and have a direct control over the voltage applied to the coils.

By substituting the voltages in the set of Equations 12, we obtain the final set of equations that govern the system:

$$\begin{cases} \dot{z} = v \\ \dot{v} = m^{-1} \left(\frac{1}{2} \frac{\partial L_1}{\partial z} I_1^2 + \frac{1}{2} \frac{\partial L_2}{\partial z} I_2^2 + mg \right) \\ \dot{I}_1 = L_1^{-1} (-R_1 I_1 + (k_1 U_1 + c_1)) \\ \dot{I}_2 = L_2^{-1} (-R_2 I_2 + (k_2 U_2 + c_2)) \end{cases} \quad (14)$$

3.2 Model Linearization

The model derived in the previous subsections (Equations 14) is highly non-linear. In order to be able to apply linear control techniques, it is necessary to linearize the model around a given operating point.

3.2.1 Operating point computation

The operating point is the set of values of the state and input around which the linearization is performed. Given the set of Equations 14, the operating point can be computed by setting the time derivatives to zero, set at least 2 of the state variables or input variables to constant values and solve the remaining equations. Based on their physical meaning, it's reasonable to set the position of the ball z and the current in the lower electromagnet I_2 . By doing so, all the other state and input variables can be computed by solving the following set of equations:

$$\mathbf{x}_{op} = \begin{bmatrix} z_{op} \\ v_{op} \\ I_{1op} \\ I_{2op} \end{bmatrix} = \begin{cases} z^* \\ 0 \\ \sqrt{-(2mg + \frac{\partial L_2}{\partial z} |_{z_{op}} I_{2op}^2) / \frac{\partial L_1}{\partial z} |_{z_{op}}} \\ I_2^* \end{cases} \quad (15)$$

$$\mathbf{u}_{op} = \begin{bmatrix} U_{1op} \\ U_{2op} \end{bmatrix} = \begin{cases} \max [0, R_{10} (I_{1op} - I_{1min}) / k_1] \\ \max [0, R_{20} (I_{2op} - I_{2min}) / k_2] \end{cases} \quad (16)$$

Where z^* is the desired position of the ball and I_2^* is the desired current in the lower electromagnet. As we can see, once those values are set, all the other states and inputs can be computed uniquely.

3.2.2 Linearized model derivation

Based on the operating point computed in the previous subsection, the linearized model can be obtained by performing a Taylor expansion around the operating point up to the first order terms of Equations 14.

Before performing the linearization, we briefly recall the general form of a Taylor expansion of a function $f(\mathbf{x})$ around a point \mathbf{x}_{op} :

$$f(\mathbf{x}) \approx f(\mathbf{x}_{op}) + \nabla f(\mathbf{x}_{op}) \cdot (\mathbf{x} - \mathbf{x}_{op}) \quad (17)$$

Where $\nabla f(\mathbf{x}_{op})$ is the gradient of $f(\mathbf{x})$ evaluated at \mathbf{x}_{op} .

By applying the Taylor expansion to the non-linear model, the linearized model can be obtained as:

$$\mathbf{f}(\mathbf{x}) - \mathbf{f}(\mathbf{x}_{op}) \approx \frac{\partial \mathbf{f}}{\partial \mathbf{x}} \Bigg|_{\mathbf{x}_{op}} \cdot (\mathbf{x} - \mathbf{x}_{op}) \quad (18)$$

Considering now the set of Equations 14, the linearized model can be obtained as:

$$\begin{cases} \dot{z} - z_{op} & \approx 1(v - v_{op}) \\ \dot{v} - v_{op} & \approx m^{-1} \left(\frac{1}{2} \frac{\partial^2 L_1}{\partial z^2} \Big|_{\mathbf{x}_{op}} (z - z_{op}) I_{1op}^2 + \frac{1}{2} \frac{\partial^2 L_2}{\partial z^2} \Big|_{\mathbf{x}_{op}} (z - z_{op}) I_{2op}^2 + \frac{\partial L_1}{\partial z} \Big|_{\mathbf{x}_{op}} I_{1op}(I_1 - I_{1op}) + \frac{\partial L_2}{\partial z} \Big|_{\mathbf{x}_{op}} I_{2op}(I_2 - I_{2op}) \right) \\ \dot{I}_1 - I_{1op} & \approx (-L_1^{-2} \frac{\partial L_1}{\partial z} (-R_1 I_1 + k_1 U_1 + c_1)) \Big|_{\mathbf{x}_{op}} (z - z_{op}) + (-L_1^{-1} R_1) \Big|_{\mathbf{x}_{op}} (I_1 - I_{1op}) + (L_1^{-1} k_1) \Big|_{\mathbf{x}_{op}} (U_1 - U_{1op}) \\ \dot{I}_2 - I_{2op} & \approx (-L_2^{-2} \frac{\partial L_2}{\partial z} (-R_2 I_2 + k_2 U_2 + c_2)) \Big|_{\mathbf{x}_{op}} (z - z_{op}) + (-L_2^{-1} R_2) \Big|_{\mathbf{x}_{op}} (I_2 - I_{2op}) + (L_2^{-1} k_2) \Big|_{\mathbf{x}_{op}} (U_2 - U_{2op}) \end{cases} \quad (19)$$

Notice that also during the linearization process, the model has been simplified by reapplying the assumptions made in the set of Equations 11.

3.3 State Space Representation

In the optics of control theory, it is useful to represent the system in the state space form. The state space representation is a mathematical model of a physical system as a set of input, output and state variables related by first-order differential equations. The state space representation is particularly useful for linear systems, as it allows to easily apply linear control techniques.

A generic nonlinear system can be represented in the state space form as:

$$\begin{aligned} \dot{\mathbf{x}} &= f(\mathbf{x}, \mathbf{u}) \\ \mathbf{y} &= g(\mathbf{x}, \mathbf{u}) \end{aligned} \quad (20)$$

Where \mathbf{x} is the state vector and \mathbf{u} is the input vector, while f and g are generic functions that describe the system dynamics and the output equations, respectively.

Similarly to what has been done in the previous subsection, we can perform a linearization of the system around an operating point to obtain the linearized state space representation in the form of:

$$\begin{aligned} \dot{\delta\mathbf{x}} &\approx A\delta\mathbf{x} + B\delta\mathbf{u} \\ \delta\mathbf{y} &\approx C\delta\mathbf{x} + D\delta\mathbf{u} \end{aligned} \quad (21)$$

Where $\delta\mathbf{x}$ and $\delta\mathbf{u}$ are the deviations of the state and input vectors from the operating point, respectively. Instead, A , B , C and D are the Jacobian matrices with respect to the state and input vectors evaluated at the operating point.

MLS state space representation Given the linearized model derived in the previous subsection (Equation 19), we can define the state vector \mathbf{x} and the input vector \mathbf{u} as:

$$\mathbf{x} = \begin{bmatrix} z \\ v \\ I_1 \\ I_2 \end{bmatrix} \quad \mathbf{u} = \begin{bmatrix} U_1 \\ U_2 \end{bmatrix} \quad (22)$$

Once the state and input vectors have been defined, the linearized state space representation can be obtained by leveraging the linearized model derived previously. The matrices A , B , C and D are then defined as:

$$\begin{aligned} A &= \frac{\partial f}{\partial \mathbf{x}} \Big|_{(\mathbf{x}_{op}, \mathbf{u}_{op})} = \begin{bmatrix} 0 & 1 & 0 & 0 \\ a_{21} & 0 & a_{23} & a_{24} \\ a_{31} & 0 & a_{33} & 0 \\ a_{41} & 0 & 0 & a_{44} \end{bmatrix} \\ B &= \frac{\partial f}{\partial \mathbf{u}} \Big|_{(\mathbf{x}_{op}, \mathbf{u}_{op})} = \begin{bmatrix} 0 & 0 \\ 0 & 0 \\ b_{31} & 0 \\ 0 & b_{42} \end{bmatrix} \\ C &= \frac{\partial g}{\partial \mathbf{x}} \Big|_{(\mathbf{x}_{op}, \mathbf{u}_{op})} = [1 \ 0 \ 0 \ 0] \\ D &= \frac{\partial g}{\partial \mathbf{u}} \Big|_{(\mathbf{x}_{op}, \mathbf{u}_{op})} = [0 \ 0] \end{aligned} \quad (23)$$

Based on Equation 19, the elements of the matrices A , B , C and D can be computed as:

$$\begin{aligned}
a_{21} &= \frac{1}{m} \left(\frac{1}{2} \frac{\partial^2 L_1}{\partial z^2} I_1^2 + \frac{1}{2} \frac{\partial^2 L_2}{\partial z^2} I_2^2 \right) \Big|_{(\mathbf{x}_{op}, \mathbf{u}_{op})} \\
a_{23} &= \frac{1}{m} \left(\frac{\partial L_1}{\partial z} I_1 \right) \Big|_{(\mathbf{x}_{op}, \mathbf{u}_{op})} \\
a_{24} &= \frac{1}{m} \left(\frac{\partial L_2}{\partial z} I_2 \right) \Big|_{(\mathbf{x}_{op}, \mathbf{u}_{op})} \\
a_{31} &= \left(-L_1^{-2} \frac{\partial L_1}{\partial z} (-R_1 I_1 + k_1 U_1 + c_1) \right) \Big|_{(\mathbf{x}_{op}, \mathbf{u}_{op})} \\
a_{33} &= (L_1^{-1}(-R_1)) \Big|_{(\mathbf{x}_{op}, \mathbf{u}_{op})} \\
a_{41} &= \left(-L_2^{-2} \frac{\partial L_2}{\partial z} (-R_2 I_2 + k_2 U_2 + c_2) \right) \Big|_{(\mathbf{x}_{op}, \mathbf{u}_{op})} \\
a_{44} &= (L_2^{-1}(-R_2)) \Big|_{(\mathbf{x}_{op}, \mathbf{u}_{op})} \\
b_{31} &= (L_1^{-1} k_1) \Big|_{(\mathbf{x}_{op}, \mathbf{u}_{op})} \\
b_{42} &= (L_2^{-1} k_2) \Big|_{(\mathbf{x}_{op}, \mathbf{u}_{op})}
\end{aligned} \tag{24}$$

3.4 Single Coil Configuration

In this section, we will present the model of the MLS system when only the upper coil is used for control purposes. This configuration is the one that will be used in the rest of the document and the laboratory activities. The choice has been taken in order to deal with a simpler SISO system, which is easier to control and analyze.

In the following, starting from Equation 14, we will at derive the reduced model, linearize it and represent it in state-space form.

Reduced Equations of Motion At first, if we consider energizing only the upper coil, we can simply remove the terms related to the lower coil from the equations of motion. Based on Equation 14, we can write the following equations:

$$\begin{cases} \dot{z} = v \\ \dot{v} = m^{-1} \left(\frac{1}{2} \frac{\partial L_1}{\partial z} I_1^2 + mg \right) \\ \dot{I}_1 = L_1^{-1} (-R_1 I_1 + (k_1 U_1 + c_1)) \end{cases} \tag{25}$$

Linearization As already discussed in Section 3.2, we can linearize via Taylor expansion the equations of motion around one of its operating points. For the case of the single coil configuration, Equations 15 and 16 reduce to:

$$\mathbf{x}_{op} = \begin{bmatrix} z_{op} \\ v_{op} \\ I_{1op} \end{bmatrix} = \begin{cases} z^* \\ 0 \\ \sqrt{-(2mg + \frac{\partial L_2}{\partial z} \Big|_{z_{op}} (\frac{V_{2min}}{R_{20}})^2) / \frac{\partial L_1}{\partial z} \Big|_{z_{op}}} \end{cases} \tag{26}$$

$$\mathbf{u}_{op} = [U_{1op}] = \left\{ \max [0, (R_{10} I_{1op} - c_1) / k_1] \right\} \tag{27}$$

By performing the Taylor expansion of Equations 25 around the operating point, we obtain the following linearized model:

$$\begin{cases} \dot{z} - z_{op} \approx 1(v - v_{op}) \\ \dot{v} - v_{op} \approx m^{-1} \left(\frac{1}{2} \frac{\partial^2 L_1}{\partial z^2} \Big|_{\mathbf{x}_{op}} (z - z_{op}) I_{1op}^2 + \frac{\partial L_1}{\partial z} \Big|_{\mathbf{x}_{op}} I_{1op}(I_1 - I_{1op}) \right) \\ \dot{I}_1 - I_{1op} \approx \left(-L_1^{-2} \frac{\partial L_1}{\partial z} (-R_1 I_1 + k_1 U_1 + c_1) \right) \Big|_{\mathbf{x}_{op}} (z - z_{op}) + \left(-L_1^{-1} R_1 \right) \Big|_{\mathbf{x}_{op}} (I_1 - I_{1op}) + \left(L_1^{-1} k_1 \right) \Big|_{\mathbf{x}_{op}} (U_1 - U_{1op}) \end{cases} \tag{28}$$

State-Space Representation Finally, we can represent the linearized model in state-space form. Given the reduction of the system to a SISO one, we need to redefine the state vector \mathbf{x} and the input vector \mathbf{u} as follows:

$$\mathbf{x} = \begin{bmatrix} z \\ v \\ I_1 \end{bmatrix} \quad \mathbf{u} = [U_1] \quad (29)$$

Once the state and input vectors have been defined, the linearized state-space representation can be obtained by leveraging the linearized model derived previously. The matrices A , B , C and D are then defined as:

$$\begin{aligned} A &= \left. \frac{\partial f}{\partial \mathbf{x}} \right|_{(\mathbf{x}_{op}, \mathbf{u}_{op})} = \begin{bmatrix} 0 & 1 & 0 \\ a_{21} & 0 & a_{23} \\ a_{31} & 0 & a_{33} \end{bmatrix} \\ B &= \left. \frac{\partial f}{\partial \mathbf{u}} \right|_{(\mathbf{x}_{op}, \mathbf{u}_{op})} = \begin{bmatrix} 0 \\ 0 \\ b_{31} \end{bmatrix} \\ C &= \left. \frac{\partial g}{\partial \mathbf{x}} \right|_{(\mathbf{x}_{op}, \mathbf{u}_{op})} = [1 \ 0 \ 0] \\ D &= \left. \frac{\partial g}{\partial \mathbf{u}} \right|_{(\mathbf{x}_{op}, \mathbf{u}_{op})} = [0] \end{aligned} \quad (30)$$

Given the non-correlation between the two coils currents, the elements of the matrices A , B , C and D remain exactly as already computed in Section 24.

4 Identification

To effectively control the system, it is crucial to identify its physical and dynamic parameters. This process involves a series of carefully designed experiments and measurements to extract reliable data.

The parameter identification process is divided into the following steps:

1. **Direct measurement:** using conventional instruments, measure physical parameters that do not require specific test setups, such as geometric dimensions or mass or static resistance of the coils.
2. **Sensor characterization:** map the relationship between the ball's position and the output voltage of the infrared sensor. Additionally, statistically analyze the output of the sensors used internally to estimate the system state.
3. **Control-to-voltage dependency:** examine the relationship between the control signal and the resulting applied voltage to the coils ($V = V(U)$).
4. **Inductance characterization:** determine parameters for inductances based on the model described in Equations 7. This involves analyzing the system's electrical response under various conditions.
5. **Force analysis:** measure the electromagnetic force applied to the ball to validate both the identified parameters and the overall model's accuracy;
6. **Active levitation:** a preliminary active controlled levitation test to further refine the identified parameters.

Except for direct measurements, all tests are performed using the data acquisition capabilities of the **Inteco** control unit itself.

To simplify the identification process, we will assume the lower and upper coils have identical parameters unless explicitly stated otherwise. This assumption allows us to streamline both the methodology and the notation by avoiding subscripts that distinguish the two coils.

In all subsequent tests, parameters are identified using measurements from the upper coil.

4.1 Direct measurement

Many of the parameters of the system can be directly measured using a scale, a caliper or a voltmeter.

Among those, we have the mass of the ball m , the radius of the ball r , the distance between the upper and lower coils h and the resistance of the coil R . Their values are reported in Table 1.

Parameter	Value	Units
g	9.81	m/s^2
m	0.06157	kg
r	0.06125/2	m
h	0.098	m
R_0	4.17	Ω

Table 1: Directly measured parameters and constants

4.2 Sensors characterization

In this subsection, we will focus on the characterization of the sensors used internally by the control unit to measure or estimate the system state.

4.2.1 Voltage to position mapping

At first, we need to create the mapping between the voltage output of the infrared sensor and the position of the ball. To do so, we simply sample the output voltage of the infrared sensor and the position of the ball using the data acquisition system included in the **Inteco** control unit and a caliper.

The obtained data is shown in Figure 5.

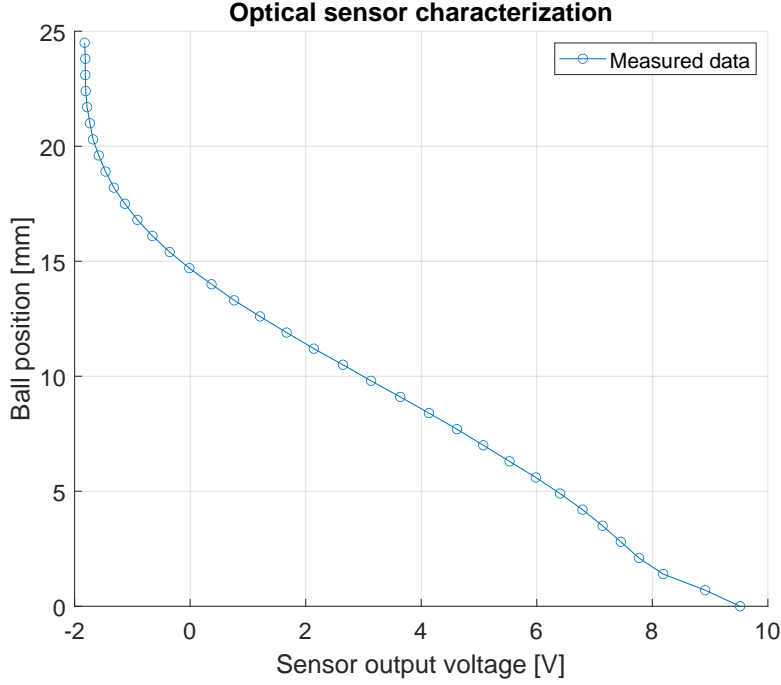


Figure 5: Position of the ball as a function of the output voltage of the infrared optical sensor.

One can clearly see the non-linear relationship between the ball's position and the output voltage of the infrared sensor.

Moreover, it's important to underline the hardware limitations of the sensor that allows a maximum measurement distance of $\approx 20[\text{mm}]$ from the upper coil before reaching its saturation limit.

4.2.2 Sensors noise analysis

A comprehensive analysis of the sensors' noise is crucial to correctly estimate both the position of the ball and the coils' current. The experimental setup consists of keeping the ball at a fixed position and recording the sensors' output for a certain amount of time imposing a zero control signal. The analysis then assumes the sensors' noise to be a zero-mean Gaussian white noise process.

With this optics, we can estimate the standard deviation for each sensor and use it to design the filters and estimators in the following sections (see Section 6).

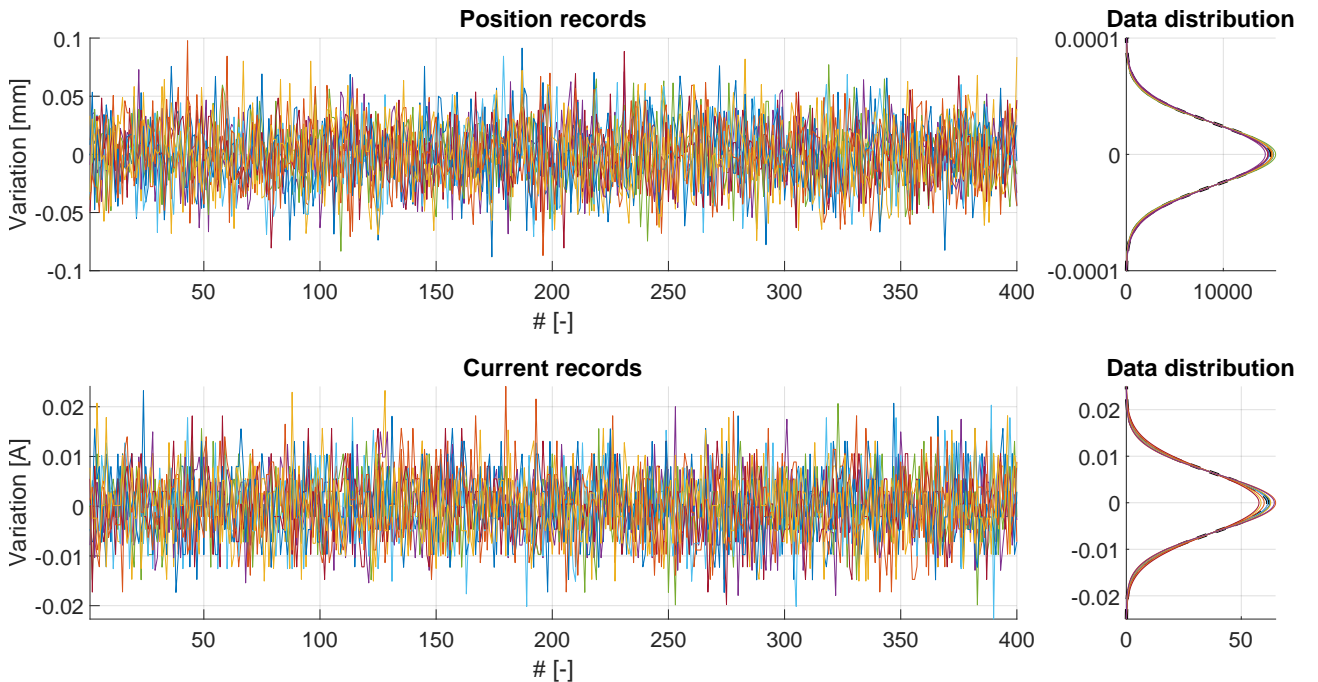


Figure 6: Sensors' noise analysis.

In Figure 6, the analysis of the sensors' noise is shown.

The left plots show the time history of the sensor output variations, while the right plots show the Gaussian distribution of the sensors' noise with the mean distribution marked with a dashed black line. The upper plots refer to the infrared sensor, while the lower plots refer to the current sensor.

The standard deviation and covariance of the sensors' noise is reported in Table 2.

Sensor	Standard deviation	Covariance
Infrared	$2.684386 \cdot 10^{-5}$ [m]	$7.209085 \cdot 10^{-10}$ [m ²]
Current	$6.482599 \cdot 10^{-3}$ [A]	$4.207942 \cdot 10^{-5}$ [A ²]

Table 2: Standard deviation and covariance of the sensors' noise.

4.3 Control to voltage

As already clarified in Section 3.1.5, what we actually control is the duty cycle of the PWM signal that is applied to the coils. However, as we saw in Equation 12, the model consider the effective voltage applied to the coils as input.

In order to use the control signal as input to the model, we need to identify the parameters of the relation between the control signal and the effective voltage applied to the coils which has already been discussed in Equation 13.

The experimental procedure to identify this relation can be summarized in the following steps:

1. Connect the control unit to the coils and to the power supply.
2. Connect the multimeter to the coils and set it to measure the voltage.
3. Set the control unit to a specific duty cycle.
4. Measure the voltage applied to the coils.
5. Repeat steps 3 and 4 for many duty cycles.

The output of this test is a series of points that can be fitted to 13 in order to identify the parameters of the relation. In Figure 7 we can observe both the measured points, the linear fitting and the effective voltage applied considering also the initial black zone.

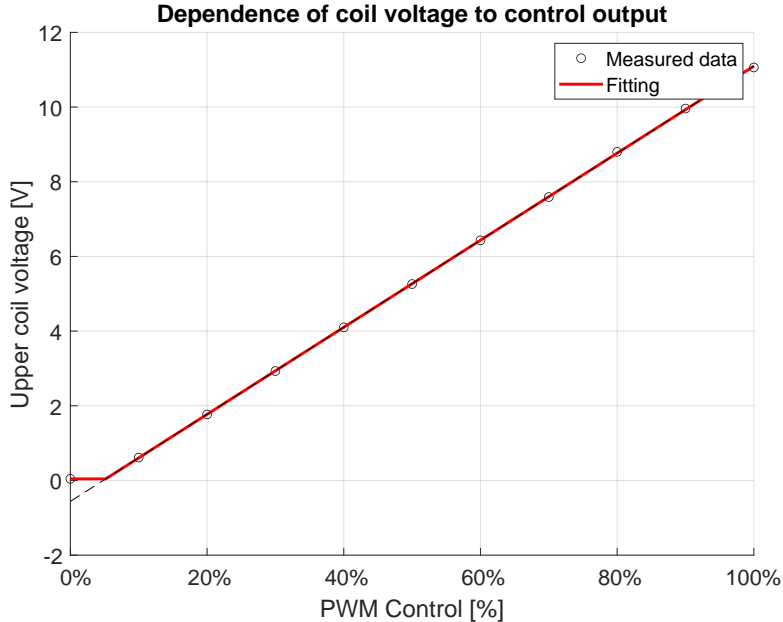


Figure 7: Control to voltage identification

As we can see, the linear model for the relation $V = f(U) = f(\text{PWM})$ is a good approximation outside the initial black zone control.

The values of the parameters for the Equation 13 are shown in Table 3. One might refer to Section 3.1.5 for an explanation of the parameters.

Parameter	Value	Units
V_{min}	$4.300000 \cdot 10^{-2}$	V
U_{min}	5.179276	%
k	$1.165800 \cdot 10^1$	V/%
c	$-5.608000 \cdot 10^{-1}$	V

Table 3: Control to voltage identification parameters

4.4 Inductances characterization

A key parameter of the system is the inductance of the coils.

As already proposed in Equation 7, the inductance of the coils cannot be considered constant and both its dependence on the current and the position of the ball must be taken into account when dealing with the MLS. In order to identify the inductance of the coils and all the parameters needed to characterize them, we have to measure $L(z, I)$ for many currents and ball positions. Once these values are known, we can fit the data to the model proposed in Equation 7 and identify its parameters.

Given a certain (fix in time) position of the ball and a certain current step input, we can measure the value of the inductance of the coils, knowing that:

$$V = RI + \frac{d(LI)}{dt} = RI + \left(\frac{\partial L}{\partial I} I + L \right) \dot{I} \quad (31)$$

If we suppose for a moment that the variation of the inductance with the current is negligible, we can obtain a closed form solution for the current in the RL circuit as follows:

$$I(t) = \frac{V_{final}}{R_0} \left(1 - e^{-\frac{R_0}{L} t} \right) \quad (32)$$

Given the previous equations, we can adopt the following strategy to fully characterize the inductance of the coils over the range of possible ball positions and currents:

1. Fix the ball at a certain height (z^*);
2. Apply a certain current step input to the system (I^*);
3. Measure the current in the coils ($I(t)$);
4. Fit the measured current to the model proposed in Equation 32 and identify $L(z^*, I^*)$;
5. Repeat from step 2 for different step inputs of currents;
6. Repeat from step 1 for different ball positions.

In Figure 8 we can see on the left all the experimental data representing the dynamics of the current in the coils for different step inputs of currents and different ball positions, while on the right we can see the fitting of some experimental data to the model proposed in Equation 32.

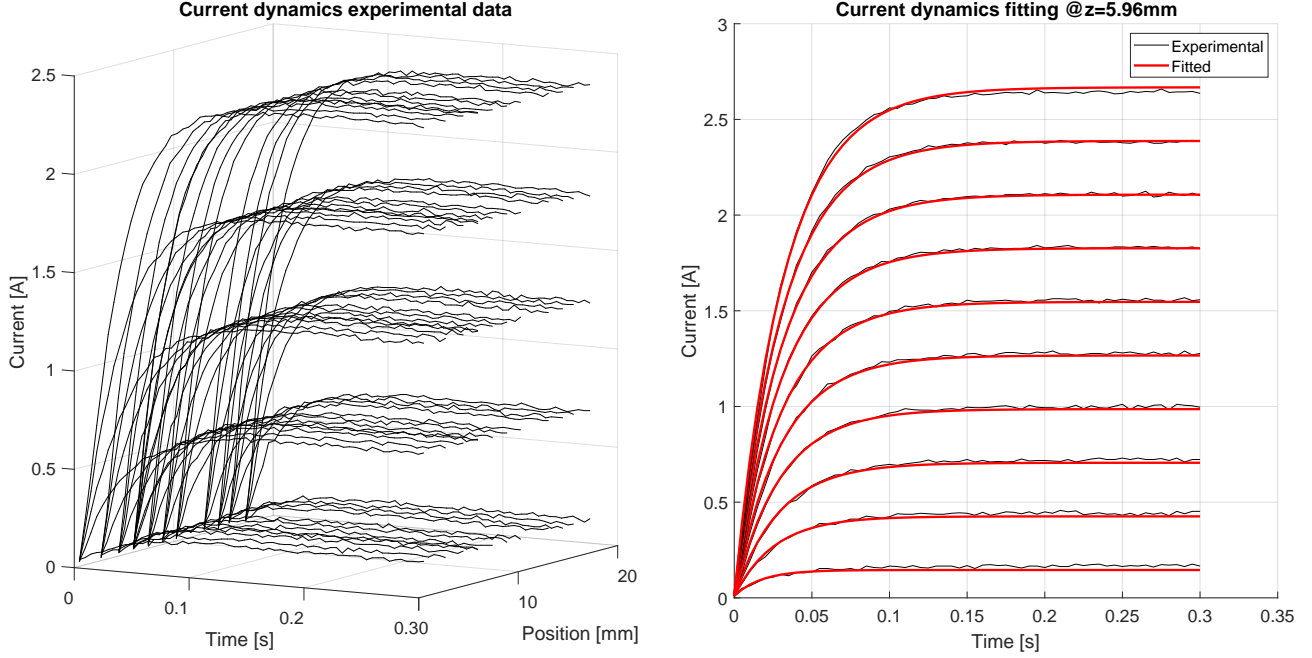


Figure 8: Inductance characterization for different currents and ball positions

From the right side of Figure 8 we can see that the fitting of the data to the model proposed in Equation 32 is optimal for middle values of the current, while it tends to underestimate and overestimate the current for low and high values of the current, respectively. This behavior is probably due to the fact that the variation of the inductance with the current that has been neglected in the model of the current (Equation 32) is not negligible and should have been taken into account.

Thanks to the data obtained from the multiple tests, we can now fit the values of the inductance of the coils to the model proposed in Equation 7 and identify its parameters. The obtained model fitting is shown in Figure 9.

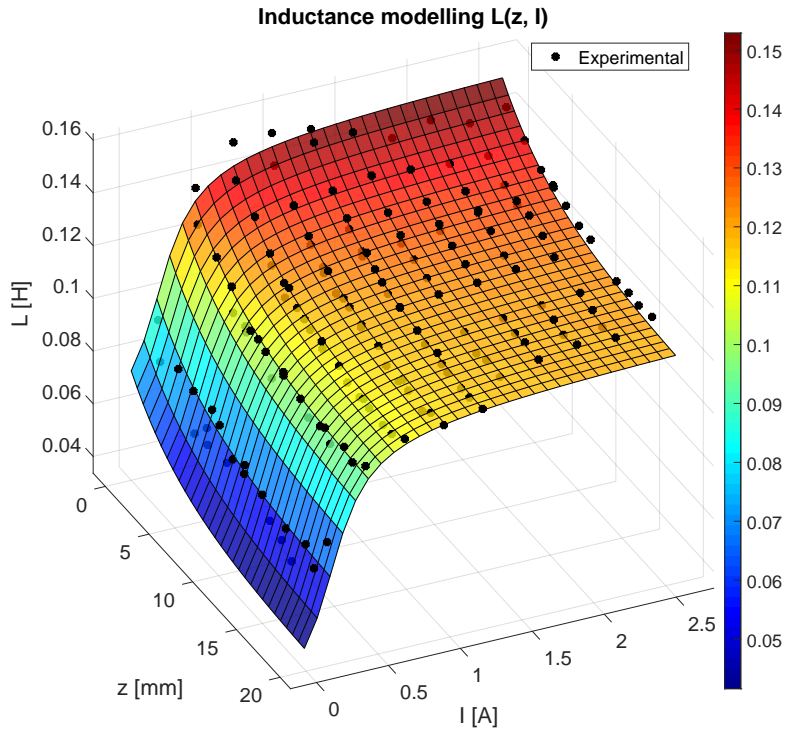


Figure 9: Inductance model fitting

The 210 black dots in Figure 9 represent the experimental data obtained from the fitting of currents dynamics for different current steps and ball positions.

The values of the parameters are shown in Table 4.

Parameter	Value	Units
L_0	$6.122809 \cdot 10^{-2}$	H
a_z	$1.837302 \cdot 10^{+2}$	$1/m$
L_z	$3.438228 \cdot 10^{-2}$	H
a_I	$4.759750 \cdot 10^{+0}$	
b_I	$6.704755 \cdot 10^{-1}$	A
L_I	$3.831209 \cdot 10^{-2}$	H

Table 4: Inductance characterization parameters

As a double check against the model proposed in Equation 7, one can also observe the R squared value of the fitting $R^2 = 0.961$, which is a good indicator of the quality of the fitting.

4.5 Force analysis

Thanks to the data obtained from the previous tests, we are already able to predict the force applied to the ball by the inductance. In particular, we already know that the electromagnetic force applied to the ball is given by the following equation:

$$F_{em} = \frac{1}{2} \frac{\partial L}{\partial z} I^2 = \frac{1}{2} (-a_z L_z e^{-a_z z}) I^2 \quad (33)$$

Because of the previously identified parameters, we have an analytical expression for the sensitivity of the inductance with respect to the position of the ball. However, due to uncertainties in the identification of the parameters, we can expect some discrepancies between the predicted force and the measured one.

In order to quantify these discrepancies and validate the model, we use a direct method to measure the force applied to the ball by the inductance and compare it with the predicted one. To do so, we recall Equation 14 and in particular the equation relative to \dot{v} :

$$\dot{v} = m^{-1} \left(\frac{1}{2} \frac{\partial L_1}{\partial z} I_1^2 + \frac{1}{2} \frac{\partial L_2}{\partial z} I_2^2 + mg \right) \quad (34)$$

If we consider the system at rest or equivalently at the incipient motion of the ball, we can simplify the equation as follows:

$$0 = \frac{1}{2} \frac{\partial L_1}{\partial z} I_1^2 + \frac{1}{2} \frac{\partial L_2}{\partial z} I_2^2 + mg \quad (35)$$

Supposing now that only the first coil is energized, we can further simplify the equation as follows:

$$0 = \frac{1}{2} \frac{\partial L_1}{\partial z} I_1^2 + mg \quad (36)$$

Which leads to:

$$\frac{\partial L_1}{\partial z} = -2 \frac{mg}{I_1^2} \quad (37)$$

This last equation basically tells us that in steady state conditions, when the ball is levitating (i.e. $\dot{z} = 0$ and not supported by any platform), the sensitivity of the inductance of the first coil has an analytical expression that can be directly evaluated by measuring the current in the first coil and the position of the ball.

In order to follow this approach, the experimental steps are as follows:

1. By regulating a lower platform, the ball is placed at a certain height (z^*);
2. A linearly increasing voltage is applied to the first coil;
3. The current circulating in the first coil is measured;
4. The current at which the ball starts to levitate is identified;
5. The sensitivity of the inductance is calculated using Equation 37.
6. The test is repeated for different initial positions of the ball.

In Figure 10 we can see both the position of the ball (red line) and the current circulating in the first coil (black line) around the identified levitation point (marked by the vertical black dashed line).

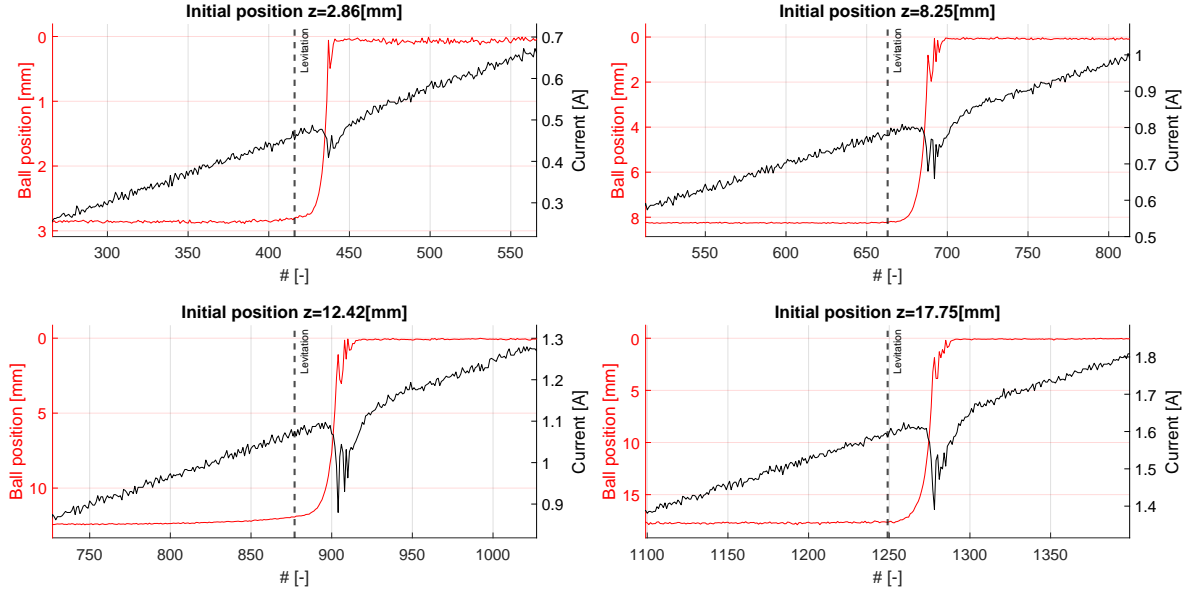


Figure 10: Position of the ball and current in the first coil around the levitation point (marked by vertical black dashed line)

Instead, in Figure 11, we can observe both the measured data and the fitted ones. On the right side figure, a complete characterization of the electromagnetic force has been reconstructed based again on the above equations.

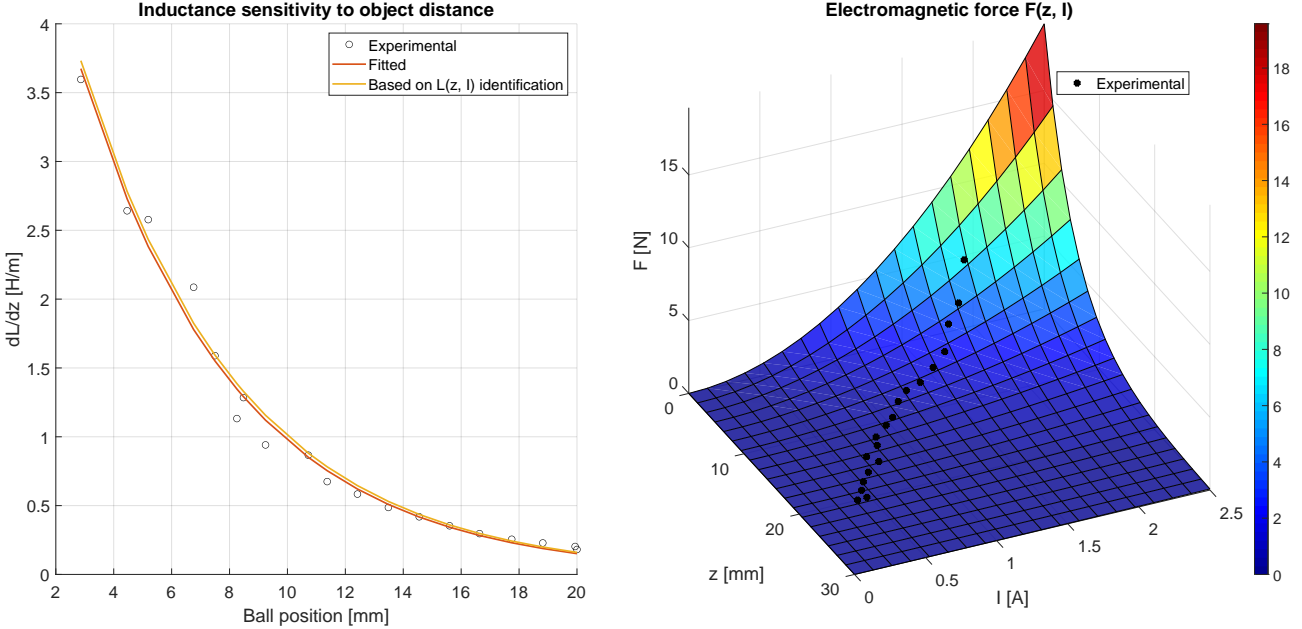


Figure 11: Dynamic inductance characteristics and electromagnet force

The left-hand side of Figure 11 shows a comparison between the measured data (black circles), their fitting (red line) and the sensitivity of the inductance coming from the parameters identified in Section 4.4 (yellow line). Data shows great accuracy in almost the entire range of the ball position.

The right-hand side of Figure 11 shows the electromagnetic force generated by the first coil as a function of both the ball position and the current circulating in the coil. One can notice that the force has an exponential behavior with respect to the ball position and a quadratic behavior with respect to the current.

4.6 Active levitation (parameters validation)

For the sake of identification, we ignore here for a moment the description of the controller used to perform the active control on the ball position given that in Section 7.1.2 we will describe the controller in detail.

The final step of the identification process is to perform an active levitation test to check that the electromagnetic force predicted by the coefficients retrieved in Section 4.4 and Section 4.5 is accurate. This test is crucial to validate the overall model and to obtain the final values of the coefficients.

The active levitation test consists of applying a control signal to the coils to maintain the ball at a fixed position. Performing the test at different ball heights and annotating the corresponding current values allows us to determine experimentally the relationship $I_{op} = I_{op}(z_{op})$. As we have already seen in Section 3.2, the relationship between the current and the ball position is given by:

$$I_{op} = \sqrt{-\left(2mg + \frac{\partial L_2}{\partial z} \Big|_{z_{op}} \left(\frac{V_{2min}}{R_{20}}\right)^2\right) / \frac{\partial L_1}{\partial z} \Big|_{z_{op}}} \approx \sqrt{-(2mg) / \frac{\partial L_1}{\partial z} \Big|_{z_{op}}} \quad (38)$$

In the left-hand side of Figure 12 we show the time evolution of the ball position during the active levitation test. One can easily see that the ball is maintained at three different heights by applying different control signals to the coils.

Instead, in the right-hand side of Figure 12, the experimentally determined operating points, their interpolation and the theoretical curve given by Equation 38 using the coefficients listed in Table 4 are shown.

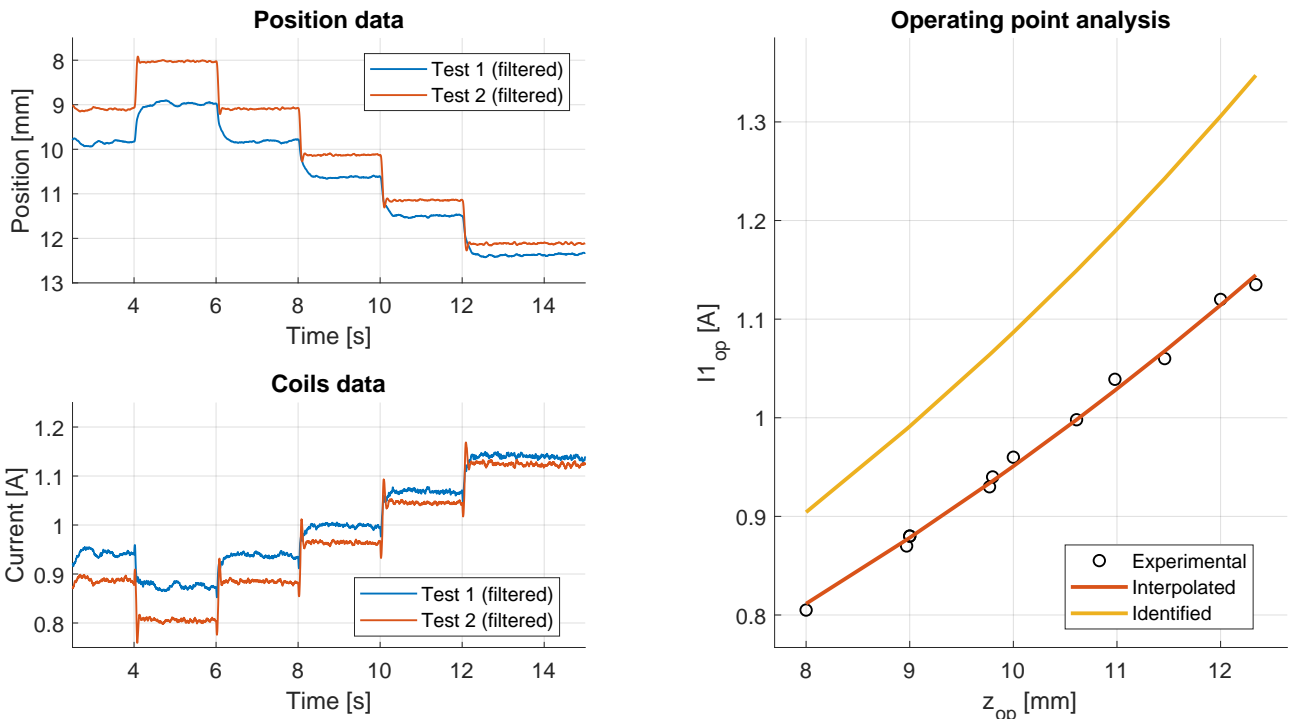


Figure 12: Comparison of the operating point between the theoretical model and the experimental data obtained during the active levitation test.

As we can see, the curve based on the parameters of Table 4 doesn't fit the experimental data as expected. The gap between the identified and the theoretical curve, might found its origin in the assumption of neglecting the term $\frac{\partial L}{\partial I} I$ in Equation 31 when fitting the current dynamics in Section 4.4 or due to poor identification of the levitation point in case of the procedure followed in Section 4.5.

In any case, given the large distance between the theoretical curve and the experimental data, we decided to discard the previously identified parameters and to re-identify them using the data obtained from the active levitation test which is considered more reliable.

The final values of the parameters are shown in Table 5.

Parameter	Value	Units
L_0	$6.539244 \cdot 10^{-2}$	H
a_z	$1.585423 \cdot 10^{+2}$	$1/m$
L_z	$4.044743 \cdot 10^{-2}$	H
a_I	$5.296552 \cdot 10^{+0}$	
b_I	$1.042271 \cdot 10^{+0}$	A
L_I	$3.288792 \cdot 10^{-2}$	H

Table 5: Final inductance parameters obtained via active levitation test.

Notice that with respect to the values presented in Table 4, only a_z and L_z have been directly obtained from the active levitation test. All the others have been re-identified by keeping fixed the values of a_z and L_z and by re-fitting the inductance model to the experimental data of currents dynamics as already described in Section 4.4.

5 Model Analysis

Given the model derived in Section 3 and the parameters identified in Section 4, we can now proceed with the analysis of the system.

As we have already discussed, the governing equations of the MLS are strongly non-linear. In order to analyze the stability of the system, we linearize the model around the operating point and derive the state-space representation of the linearized model as already discussed in Section 3.4.

For the successive analysis, we consider the following operating point:

$$\mathbf{x}_{op} = \begin{bmatrix} z_{op} \\ v_{op} \\ I_{1op} \end{bmatrix} = \begin{cases} z^* = 10 \cdot 10^{-3} \\ v^* = 0 \\ \sqrt{-(2mg)/\frac{\partial L_1}{\partial z}}|_{z_{op}} \approx 0.95 \end{cases} \quad (39)$$

$$\mathbf{u}_{op} = [U_{1op}] = \left\{ \max [0, R_{10} (I_{1op} - I_{1min}) / k_1] \right\} \approx 0.39 \quad (40)$$

At these conditions, the system matrices A , B , C and D are given as follows:

$$A = \begin{bmatrix} 0 & 1 & 0 \\ 1555 & 0 & -20.63 \\ 0 & 0 & -35.55 \end{bmatrix} \quad B = \begin{bmatrix} 0 \\ 0 \\ 99.41 \end{bmatrix} \quad (41)$$

$$C = [1 \ 0 \ 0] \quad D = [0] \quad (42)$$

5.1 Controllability and observability

The controllability and observability of the system are crucial aspects to consider when designing a control strategy. Controllability ensures that the system's state can be manipulated by the control inputs, while observability guarantees that the state can be accurately estimated from the system's outputs.

The controllability matrix $\mathcal{K}\mathcal{R}$ and observability matrix $\mathcal{K}\mathcal{O}$ are defined as follows:

$$\begin{aligned} \mathcal{K}\mathcal{R} &= [B \ AB \ A^2B] \\ \mathcal{K}\mathcal{O} &= [C^T \ (CA)^T \ (CA^2)^T] \end{aligned} \quad (43)$$

By computing the rank of the controllability and observability matrices, we can determine whether the system is controllable and observable. In particular, based on the Kalman's reachability and observability conditions, the system is controllable if and only if $\text{rank}(\mathcal{K}\mathcal{R}) = n$ and observable if and only if $\text{rank}(\mathcal{K}\mathcal{O}) = n$, where n is the number of states in the system.

An explicit computation shows that the system is both controllable and observable, given that:

$$\mathcal{K}\mathcal{R} \approx 10^5 \begin{bmatrix} 0 & 0 & -0.0205 \\ 0 & -0.0205 & 0.7294 \\ 0.0010 & -0.0353 & 1.2570 \end{bmatrix} \quad \mathcal{K}\mathcal{O} \approx 10^3 \begin{bmatrix} 0.0010 & 0 & 0 \\ 0 & 0.0010 & 0 \\ 1.5553 & 0 & -0.0206 \end{bmatrix} \quad (44)$$

5.2 Open loop stability

The stability of the system can be assessed by analyzing the poles of the open-loop system, which corresponds to the eigenvalues of the system matrix A . By solving the characteristic equation, we find that the poles of the system are located at:

$$\text{eig}(A) = \begin{cases} 39.44 \\ -39.44 \\ -35.56 \end{cases} \quad (45)$$

One can clearly notice that one of the poles is located on the right-hand side of the complex plane, indicating that the system is inherently unstable.

Root Locus Considering the unstable nature of the system, we perform a root locus analysis to identify potential proportional gains that achieve a stable closed-loop system. The root locus plot is shown in Figure 13.

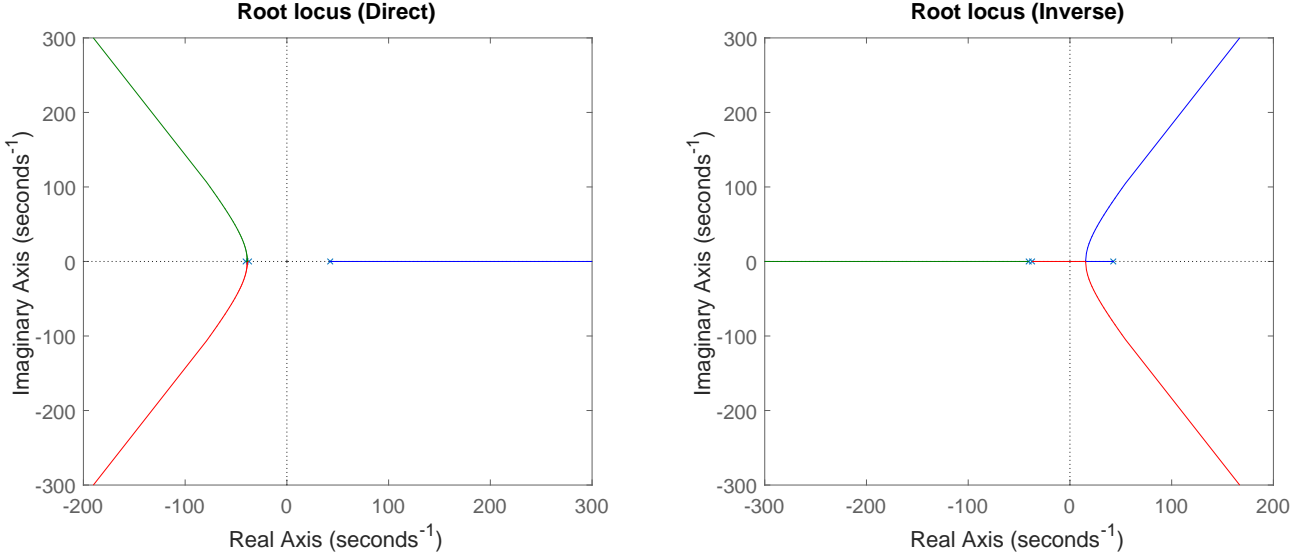


Figure 13: Root Locus plot of the open loop system with direct and inverse proportional control.

The root locus plot illustrates how the system poles migrate in the complex plane as the proportional gain of the controller is varied.

Again, we observe that one of the three poles is unstable, and we also notice that a simple proportional controller is not sufficient to stabilize the system, as the unstable poles do not move to the left-hand side of the complex plane for any value of the gain K .

Bode Diagram To further analyze the stability of the system, we consider the Bode plot for the open-loop transfer function. The Bode diagram is shown in Figure 14.

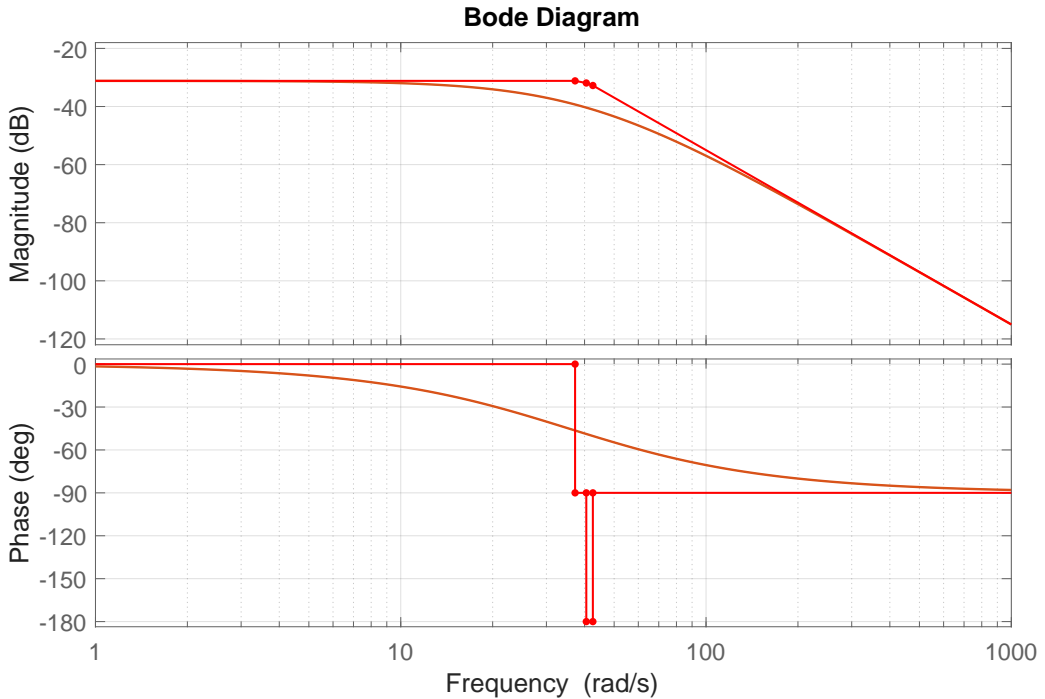


Figure 14: Bode plot of the open loop system.

Again, we observe that the system is unstable, as the gain margin is negative.

5.3 Levitation region

From the analysis performed in Section 4.5, we can derive the levitation region of the system in which it's possible to maintain the ball in a levitated state provided that the force from the upper coil is greater than the gravitational force acting on the ball.

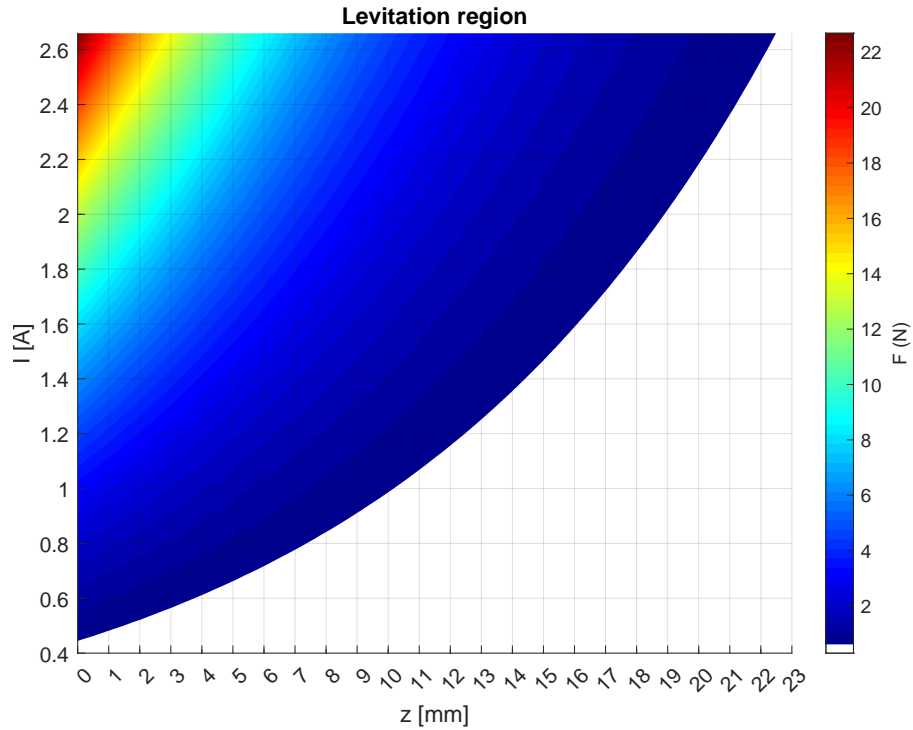


Figure 15: Levitation Region

From Figure 15, it's also possible to see that the maximum distance from the upper coils before the ball falls is $z_{max} = 22.97[\text{mm}]$ at values of the current equal to $I_{max} = 2.66[\text{A}]$.

6 Filters & Estimators Design

In this section, we will design filters and estimators to be used in the control loop of the MLS. The main goal of these filters and estimators is to reduce the noise present in the sensors' measurements and to estimate the states of the system that are not directly measurable.

In particular, we will design a low-pass filter, a Luenberger observer, a Kalman filter, and an Extended Kalman filter.

6.1 Low Pass Filter

The low pass filter is a filter that allows the low frequency components of a signal to pass through, while attenuating the high frequency components. By correctly choosing the cut-off frequency of the filter, it's possible to remove the noise from the signal, while preserving the useful information.

The transfer function of a first order low pass filter is given by:

$$G(s) = \frac{1}{\tau s + 1} \quad (46)$$

Where τ is the time constant of the filter, and it's related to the cut-off frequency ω_c by the relation $\tau = \frac{1}{\omega_c}$.

Filter on position From the Inteco manual, we have understood that the vertical velocity of the ball is computed via numerical discretization of the position. This also means that the noise present in the position measurement is amplified by the differentiation process. To reduce this noise, we design a low pass filter to be applied to the position measurements before the differentiation.

From the Bode plot of Figure 14, we can observe that the bandwidth of system (computed as the frequency at which a reduction of 3dB happens) is around:

$$\omega_n = \frac{2\pi}{T_p} \approx 20 \text{ rad/s} \quad (47)$$

As rule of thumb, we choose the cut-off frequency of the filter to be one decade after the natural frequency of the system, i.e. $\omega_c = 10\omega_n \approx 200 \text{ rad/s}$.

By doing so, we obtain the time constant of the filter to be $\tau = \frac{1}{200} = 5 \text{ ms}$ and a corresponding phase delay of:

$$\phi = -\arctan(\omega_n \tau) = -\arctan(20 \cdot 5 \cdot 10^{-3}) \approx -5.7^\circ \quad (48)$$

Filter on current The current measurement is also affected by noise. However, based on experiments, we have observed that even a slight delay in the current measurement can lead to instability of the system. Therefore, we choose not to apply a low pass filter to the current measurements.

6.2 Luenberger Observer

The Luenberger observer is a state observer that allows to estimate the state of a system, given the input coming from the controllers and at least one measured output. The observer is designed in such a way that the error between the estimated state and the real state converges to zero, as time goes to infinity.

To do so, one can consider the following dynamical system:

$$\begin{cases} \dot{\hat{x}} = A\hat{x} + Bu + L(y - C\hat{x}) \\ \hat{y} = C\hat{x} \end{cases} \quad (49)$$

Where \hat{x} is the estimated state, \hat{y} is the estimated output, L is the observer gain, and y is the measured output of the system.

The poles of the observer are given by the eigenvalues of the matrix $A - LC$, and the observer is stable if the poles are placed in the left half plane of the complex plane.

The observer gain L can be computed using the Ackermann formula, which is a generalization of the pole placement method for state-space systems.

Design Given that there are no restrictions (except for being in the left-hand side of the complex plane) for the position of the poles, we choose by chance the followings:

$$\text{eig}(A - LC) = \begin{bmatrix} -500 \\ -400 \\ -400 \end{bmatrix} \quad (50)$$

Leading to the following observer gain:

$$L = \begin{bmatrix} 900.00 & 0 \\ 201555.32 & -20.63 \\ 0 & 364.44 \end{bmatrix} \quad (51)$$

6.3 Kalman Filter

The Kalman Filter is a powerful algorithm used for estimating the state of a dynamic system from a series of noisy measurements. It is widely used in control systems, robotics, signal processing, and navigation due to its ability to provide real-time, optimal state estimates by considering system dynamics and measurement noise. One of the key strengths of the Kalman Filter is the ability to provide smooth state estimates without introducing delays.

Mathematically, the filter assumes a linear system model of the form:

$$\begin{aligned} \dot{x} &= Ax + Bu + Gw \\ y &= Cx + Du + v \end{aligned} \quad (52)$$

Where x is the state vector, u is the control input, y is the measurement, A , B , C and D are the system matrices, G is the input noise matrix, and w and v are process and white measurement noise, respectively. Among the assumptions of the Kalman filter, both the process and measurement noise are assumed to be zero-mean Gaussian white noise with known covariance Q and R .

Supposing that the system is observable, covariances Q and R are known, one can compute the Kalman gain as:

$$L = PC^T(CPC^T + R)^{-1} \quad (53)$$

Where P is the solution to the algebraic Riccati equation:

$$AP + PA^T - PC^T(CPC^T + R)^{-1}CP + Q = 0 \quad (54)$$

The Kalman gain is then used to correct the predicted state estimate based on the measurement. The corrected state estimate is given by:

$$\begin{cases} \dot{\hat{x}} = A\hat{x} + Bu + K(y - C\hat{x}) \\ \hat{y} = C\hat{x} \end{cases} \quad (55)$$

Design As we have already seen in the Luenberger observer design, the poles of the observer are given by the eigenvalues of the matrix $A - KC$, and the observer is stable if the poles are placed in the left half plane of the complex plane. The Kalman gain K can be computed using Equation 53, considering as Q and R the following matrices:

$$Q = \begin{bmatrix} 10 & 0 \\ 0 & 10 \end{bmatrix} \quad R = \begin{bmatrix} 7.21 \cdot 10^{-10} & 0 \\ 0 & 4.21 \cdot 10^{-5} \end{bmatrix} \quad (56)$$

By doing so, we obtain the following K matrix:

$$K \approx \begin{bmatrix} 487 & -0 \\ 119069 & -15 \\ -911 & 453 \end{bmatrix} \quad (57)$$

The eigenvalues of the matrix $A - KC$ are given by:

$$\text{eig}(A - KC) = \begin{bmatrix} -243.94 + 240.82i \\ -243.94 - 240.82i \\ -488.87 + 0i \end{bmatrix} \quad (58)$$

6.4 Extended Kalman Filter

The extended Kalman filter (EKF) is the nonlinear version of the Kalman filter which linearizes about an estimate of the current mean and covariance. Same assumptions done for the Kalman filter hold for the EKF, expect for the linearity of the system model.

The extended Kalman filter is a recursive state estimator for nonlinear systems. It recomputes on the fly (online) the system matrices based on the current state estimate. Once the system matrices are recomputed, the Kalman gain is computed again based on Equation 53, where now P is the solution to the Riccati equation:

$$\dot{P} = AP + PA^T - PC^T(CPC^T + R)^{-1}CP + Q \quad (59)$$

Notice that, unlike its linear counterpart, the extended Kalman filter it's not inherently an optimal estimator. It only becomes optimal in cases where both the measurement model and the state transition model are linear, as under those conditions, the EKF effectively reduces to the standard Kalman filter.

Furthermore, if the initial state estimate is inaccurate or if the process is poorly modeled, the EKF may diverge rapidly because of the inherent approximations introduced by its linearization approach.

Another challenge associated with the EKF is that its estimated covariance matrix often underrepresents the true covariance matrix. This underestimation can lead to statistical inconsistency unless corrective measures are applied, such as the introduction of "stabilizing noise."

Design The design of the EKF is similar to the Kalman filter with the key difference that the gain matrix K_k is computed online at each time step t_k based on the current state estimate \hat{x}_k .

7 Controllers Design

In this section, we move onto the design of the controllers that will be used to control the system. As we have clarified in the previous modelling section (Section 3), the system is highly nonlinear with respect to both position and current, and we control it by acting on the input PWM signal. In the following, we will present three main families of controllers that have been adopted for the control of the system:

- **PID Controllers:** a simple controller that uses the error signal, its history and derivative to compute the control signal (Section 7.1)
- **LQR Controllers:** a controller that minimizes a quadratic cost function to compute the control signal (Section 7.2)
- **MPC Controllers:** a controller that predicts the future evolution of the system and computes the control signal by minimizing a cost function (Section 7.3)

For each of these controllers, we will briefly present their theoretical background, the design choices that have been made and assess their stability by means of Bode diagrams and Root Locus plots (when possible), or by means of eigenvalues analysis. Experimental step responses (ranging from 10[mm] to 12[mm]) will also be shown as a proof of controller stability in the nearby of the linearization point.

Notice that both stability and step responses are evaluated considering the linearized model at a distance of 10[mm] from the upper coil.

Results and comparisons between the different controllers will be presented in the next section (Section 8).

7.1 PID Controllers

The Proportional-Integral-Derivative (PID) controller is a simple controller that uses the error signal, its history and derivative to compute the control signal. It is a widely used controller in industry due to its simplicity and effectiveness in many applications.

The PID controller is defined by the following equation:

$$u(t) = K_p e(t) + K_i \int_0^t e(\tau) d\tau + K_d \frac{de(t)}{dt} = K_p \left(e(t) + \frac{1}{T_i} \int_0^t e(\tau) d\tau + T_d \frac{de(t)}{dt} \right) \quad (60)$$

Where K_p , K_i and K_d are the proportional, integral and derivative gains, respectively, $e(t)$ is the error signal, and T_i and T_d instead are the integral and derivative time constants, respectively.

7.1.1 PID classical

In its simplest form, the PID is a linear controller whose three gains are tuned based on the linearization of the system. The controller gains are briefly described as follows: the proportional term K_p provides an output proportional to the current error $e(t)$ and it helps to reduce it; the integral contribution K_i accumulates the error over time to address any residual offset (steady-state error) that the proportional term cannot eliminate, and eventually it ensures the system to reach the set-point; finally, the derivative K_d reacts to the rate of change of the error, predicting future behavior and adding damping to the system, and eventually it reduces overshoot and improves stability by anticipating changes.

Design Several gain parameters have been tested to find the optimal behavior for the considered system. A first estimate has been made observing the Bode diagram, whereas a better approximation of the parameters has been obtained using the Root Locus. T_i and T_d were kept constant while changing K_p . The gain parameters used to build the transfer function are reported below:

$$K_p = -150 \quad K_i = -450 \quad K_d = -6.82 \quad (61)$$

Bode Diagram The final plots are presented in Figure 16. Compared to Figure 14, improvements on the behavior can be observed due to the application of the PID controller which tends to stabilize the system.

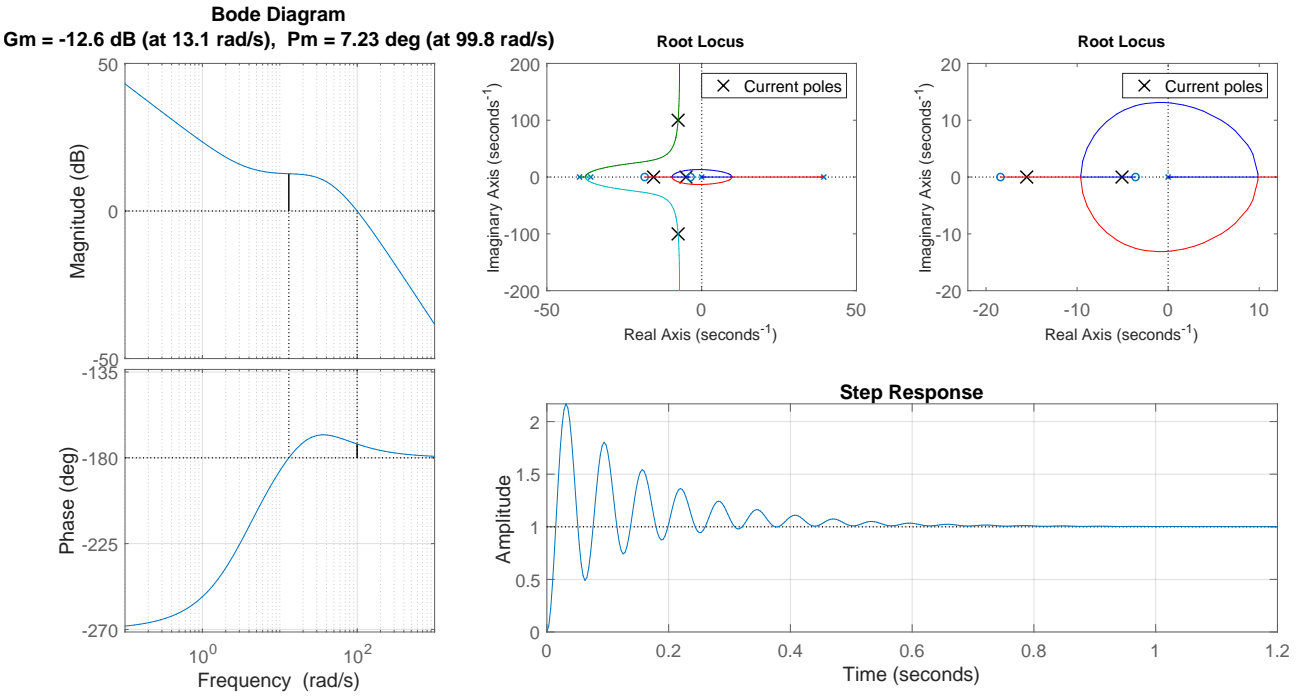


Figure 16: Bode Plot, Root Locus and Step Response (PID classic)

Eigenvalues of the system matrix have been computed since eigenvalues with negative real parts indicate stability, as well as a positive phase margin. Indeed, the resulting system is overall stable. Nevertheless, the experimental results obtained from the physical tests were not as expected. A potential explanation could be that the classical PID may introduce some issues due to the integral path and the non-linearity of the system. We have thus considered two expansions of the classical PID that bring improvements on the control of the system, that are the anti-windup (Section 7.1.2) and the gain scheduling (Section 7.1.3).

7.1.2 PID with Anti-Windup correction

The Anti-windup variation of the PID is introduced in order to avoid the windup of the integration path when the saturation of the actuator occurs. The integrator windup occurs when the actuator saturates and the integration part makes the error signal to increase. This causes the degradation of the rise time of the step response, and possibly leading to higher overshoot.

The basic idea to avoid these issues is to apply a conditional integration. The controller output is thus compared with the limits, and whenever there is some indication that saturation causes error accumulation, the integrator in PID controller is turned off.

Step Response Figure 17 shows the response of the system state to a reference step input. The stability of the dynamics can be observed, specifically considering the most relevant parameters such as the position of the sphere and the current flowing through the coils. The analytical procedure is the same as for the classical PID, and thus the controller gains that have been used are the ones described in Section 7.1.1.

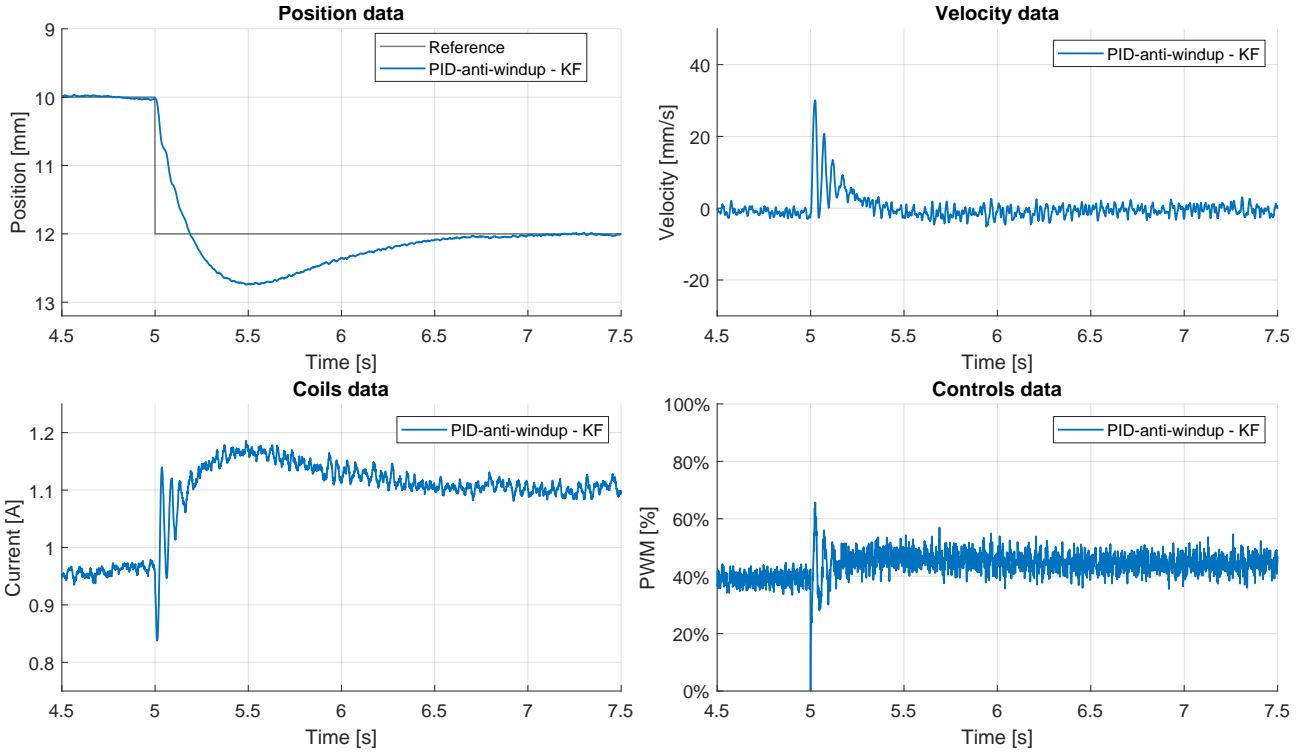


Figure 17: Step Response (PID anti-windup)

7.1.3 PID with gain scheduling

Gain scheduling is usually used for highly non-linear systems due to the ease of the implementation and its affordability. This method tunes PID controllers for a series of steady-state operating points of the plant. In the considered system, the space interval where the sphere moves has been divided into several points that represent our steady-state operating conditions, and the state-space system has been linearized at each operating condition. The set of operating conditions has to be large enough in order to get good performance everywhere, as well as the structure and the stability of the model changes when the sphere moves within the range of positions. As a second step, the controller gains have been tuned for each of these operating points. The controller develops a set of curves that gradually change the gain parameters from one operating position to another. In this way the sphere can move within the overall space range.

Bode Diagram Several curves describing the system behavior corresponding to each operating point have been plotted in order to discuss the stability conditions. Table 6 reports the gain parameters for each of the selected operating points.

$z [mm]$	K_p	K_i	K_d
5	-102	-306	-4.64
8	-136	-408	-6.18
12	-183	-550	-8.34
16	-250	-750	-11.4
20	-342	-1030	-15.5

Table 6: PID controller gains

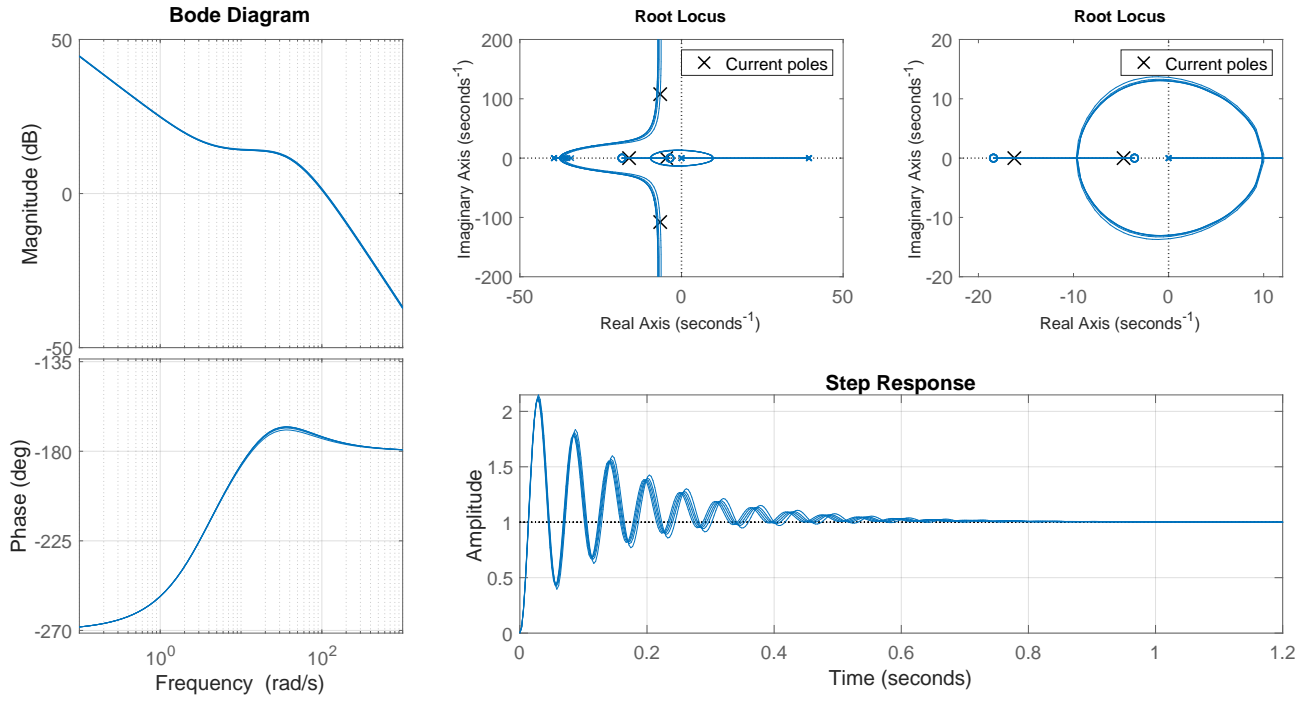


Figure 18: Bode plot, Root Locus and Step Response (PID gain scheduling)

Step Response The efficiency of the response of the system state to a reference step input is described in Figure 19.

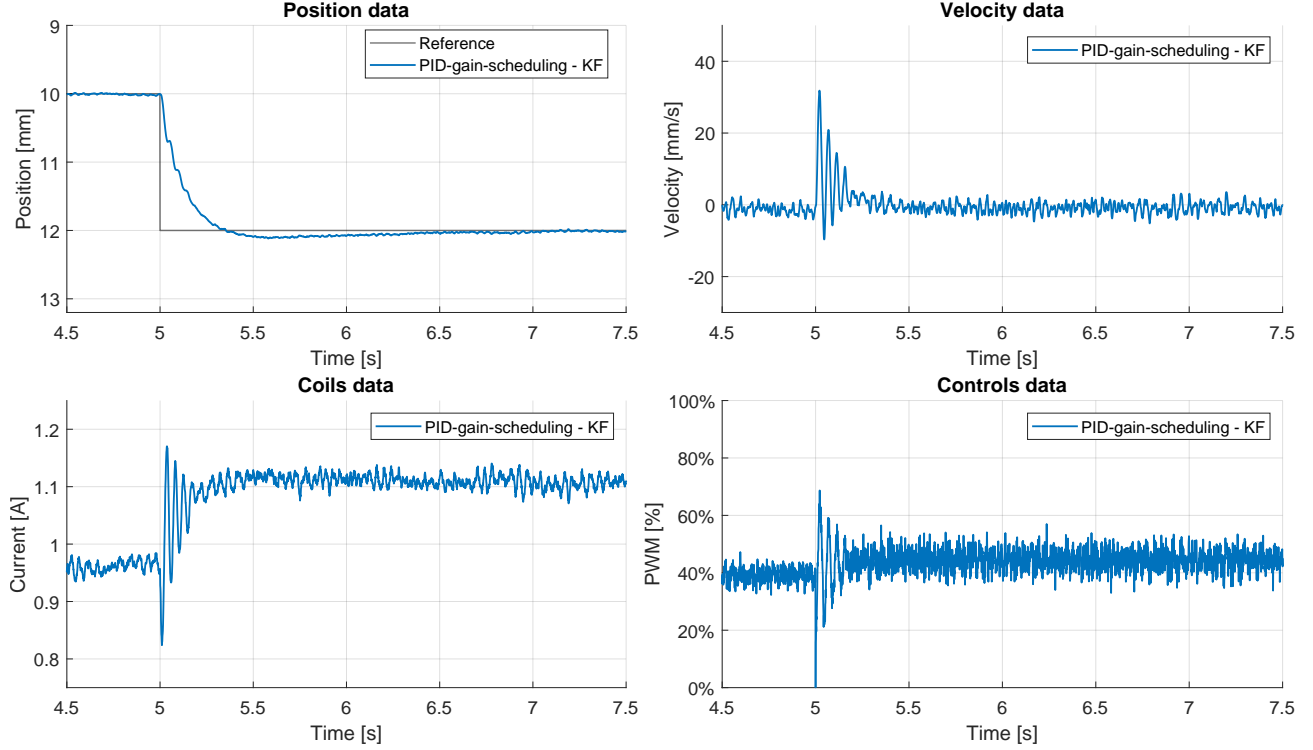


Figure 19: Step Response (PID gain scheduling)

7.2 LQ Controllers

Linear Quadratic (LQ) Controllers are optimal controllers that use state-space representation. These kinds of models minimize a quadratic cost function that balances state performance and control effort, providing a systematic way to design efficient and stable controllers.

Hereafter the Linear Quadratic Regulator (LQR), its expansion with tracking and Linear Quadratic Integrator (LQI) are taken into account to develop a stable controller for our system.

7.2.1 LQR

The Linear Quadratic Regulator (LQR) is a full state feedback controller. In order to provide the optimal control to the system, the controller aims to minimize the cost function \mathcal{J} (Equation 62). The feedback control gain matrix \mathbf{K} is thus computed considering the closed-loop characteristics that are relevant to us, specifically how efficient must be the and how much effort can be spent to get the desired performance.

The cost function which we aim to minimize is \mathcal{J} :

$$\mathcal{J} = \int_0^\infty \mathbf{x}(t)^\top \mathbf{Q} \mathbf{x}(t) + \mathbf{u}(t)^\top \mathbf{R} \mathbf{u}(t) dt, \quad (62)$$

where \mathbf{Q} is a positive semi-definite matrix penalizing state deviations from the desired state, and \mathbf{R} is a positive semi-definite matrix penalizing control effort.

The optimal control input is given by:

$$\mathbf{u}(t) = -\mathbf{K}\mathbf{x}(t), \quad (63)$$

where the feedback gain \mathbf{K} is determined by solving the Algebraic Riccati Equation:

$$\mathbf{A}^\top \mathbf{P} + \mathbf{P} \mathbf{A} - \mathbf{P} \mathbf{B} \mathbf{R}^{-1} \mathbf{B}^\top \mathbf{P} + \mathbf{Q} = 0, \quad (64)$$

where \mathbf{P} is the positive semi-definite solution to the ARE.

Once \mathbf{P} is computed, the feedback gain matrix K is:

$$\mathbf{K} = \mathbf{R}^{-1} \mathbf{B}^\top \mathbf{P}. \quad (65)$$

The closed-loop system dynamics under the LQR controller are:

$$\dot{\mathbf{x}}(t) = (\mathbf{A} - \mathbf{B}\mathbf{K})\mathbf{x}(t). \quad (66)$$

Design In order to develop an efficient controller, a great attention has been posed on the estimation of the matrices \mathbf{Q} and \mathbf{R} . As far as concerned the \mathbf{Q} matrix, the main relevance was attributed on the values that influence the state position and a moderate relevance on the values that influence the control input. Moreover, some values for R have been estimated considering inherent literature parameters.

$$\mathbf{Q} = \begin{bmatrix} 25e^3 & 0 & 0 \\ 0 & 0 & 0 \\ 0 & 0 & 16e^{-2} \end{bmatrix} \quad \mathbf{R} = 0.5 \quad (67)$$

Under these assumptions the following gain matrix has been computed.

$$\mathbf{K} = [-371.72 \quad -7.53 \quad 1.53] \quad (68)$$

The poles of the system have been computed in order to analyze its stability:

$$eig(\mathbf{A} - \mathbf{B}\mathbf{K}) = \begin{bmatrix} -47.51 + 52.95i \\ -47.51 - 52.95i \\ -92.90 + 0i \end{bmatrix} \quad (69)$$

Since eigenvalues of matrix $(\mathbf{A} - \mathbf{B}\mathbf{K})$ are situated in left hand-side plan, the resulting system is stable. Nevertheless, this control strategy has some limitations that restrict its effectiveness. Indeed, LQR does not inherently provide steady-state error correction for systems with constant disturbances or setpoint changes. It was thus impossible to make the system follows a reference input as in the other examples. In order to do that, some extensions of this simpler controller have been developed and reported in the next sections.

7.2.2 LQR with tracking capabilities

The Linear Quadratic Regulator (LQR) with tracking capabilities extends the classical LQR framework to manage systems where the goal is not only to stabilize the system but also to ensure it follows a desired trajectory or reaches a specified setpoint. This advanced control strategy is particularly useful in applications involving reference tracking, where the control objective dynamically changes over time.

To account for tracking, the state-space representation is augmented to include the tracking error:

$$\mathbf{z} = \begin{bmatrix} \mathbf{x} \\ \mathbf{e} \end{bmatrix}, \quad (70)$$

where \mathbf{x} is the system state vector, and \mathbf{e} is the error between the system state and the desired reference trajectory.

The cost function for the LQR with tracking is defined as:

$$\mathcal{J} = \int_0^\infty (\mathbf{z}^\top \mathbf{Q}_z \mathbf{z} + \mathbf{u}^\top \mathbf{R} \mathbf{u}) dt, \quad (71)$$

where \mathbf{Q}_z is the positive semi-definite weighting matrix for the augmented state, and \mathbf{R} is a positive definite weighting matrix for the control input.

The augmented system dynamics are given by:

$$\dot{\mathbf{z}} = \mathbf{A}_z \mathbf{z} + \mathbf{B}_z \mathbf{u}, \quad (72)$$

where \mathbf{A}_z and \mathbf{B}_z are derived from the original state-space model:

$$\mathbf{A}_z = \begin{bmatrix} A & 0 \\ -A_{\text{ref}} & 0 \end{bmatrix}, \quad \mathbf{B}_z = \begin{bmatrix} B \\ 0 \end{bmatrix}. \quad (73)$$

The optimal control law is derived as:

$$\mathbf{u}(t) = -\mathbf{K}\mathbf{z}(t), \quad (74)$$

where \mathbf{K} is the feedback gain matrix, computed by solving the Riccati equation for the augmented system:

$$\mathbf{P}_z \mathbf{A}_z + \mathbf{A}_z^\top \mathbf{P}_z - \mathbf{P}_z \mathbf{B}_z \mathbf{R}^{-1} \mathbf{B}_z^\top \mathbf{P}_z + \mathbf{Q}_z = 0. \quad (75)$$

This approach ensures accurate reference tracking, balances control effort and tracking performance through the tuning of \mathbf{Q}_z and \mathbf{R} , and is robust to disturbances and modeling inaccuracies.

Design The LQR with reference tracking has been developed using the same matrices \mathbf{Q} and \mathbf{R} described in Subsection 7.2.1, with the addition of the part related to the tracking error.

Step Response The experimental data measured from system controlled by LQR tracking are reported below. The reference state is followed observing a small gap after the application of the step signal.

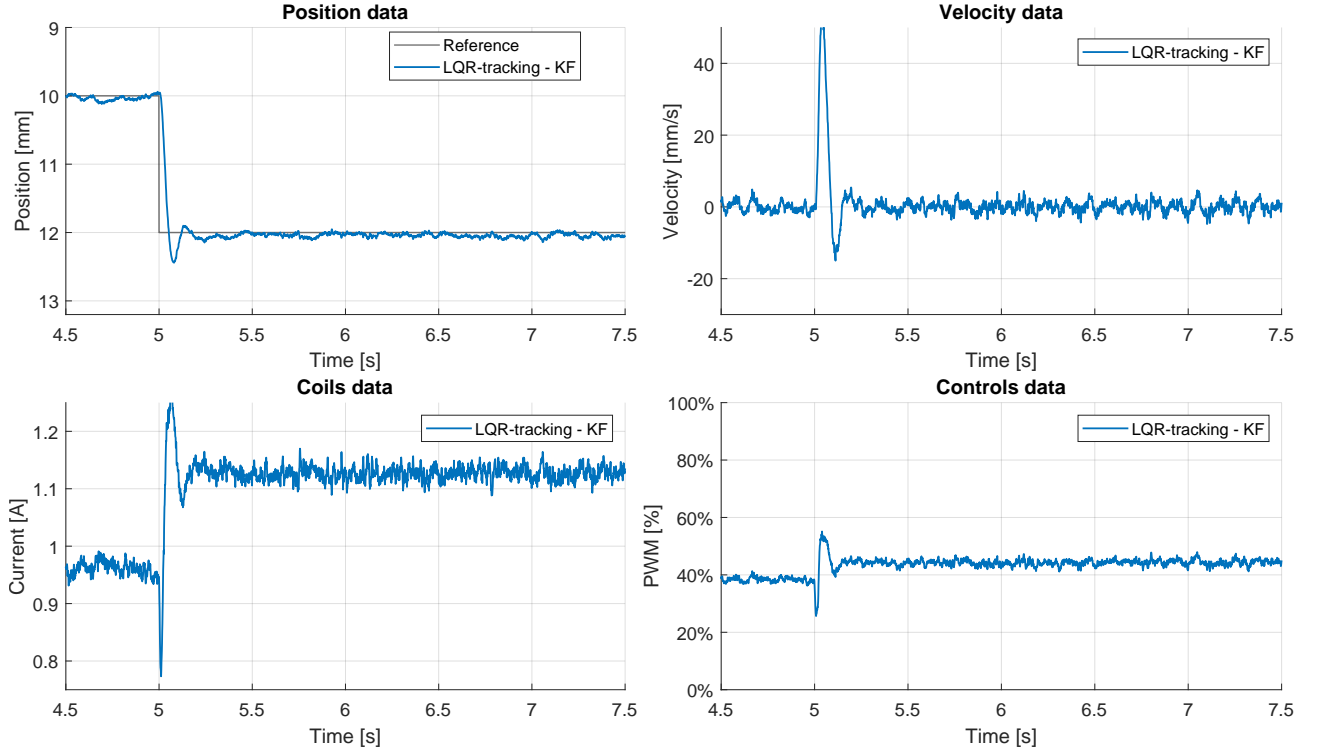


Figure 20: Step Response

7.2.3 LQI

The Linear Quadratic Integrator (LQI) is an extension of the classical LQR to achieve reference tracking and disturbance rejection by augmenting the system with integral states. Below are the key equations involved. The augmented state-space model includes the integral of the output error:

$$\begin{aligned}\dot{\mathbf{x}}(t) &= \mathbf{A}\mathbf{x}(t) + \mathbf{B}\mathbf{u}(t), \\ \dot{\mathbf{z}}(t) &= \mathbf{C}\mathbf{x}(t) - \mathbf{r}(t),\end{aligned}\tag{76}$$

where $\mathbf{x}(t)$ is the state vector, $\mathbf{u}(t)$ is the control input, $\mathbf{r}(t)$ is the reference signal, and $\mathbf{z}(t)$ is the integral of the tracking error.

The augmented system can be written as:

$$\begin{bmatrix} \dot{\mathbf{x}}(t) \\ \dot{\mathbf{z}}(t) \end{bmatrix} = \begin{bmatrix} \mathbf{A} & 0 \\ \mathbf{C} & 0 \end{bmatrix} \begin{bmatrix} \mathbf{x}(t) \\ \mathbf{z}(t) \end{bmatrix} + \begin{bmatrix} \mathbf{B} \\ 0 \end{bmatrix} \mathbf{u}(t).\tag{77}$$

The cost function to be minimized is:

$$J = \int_0^\infty \left(\begin{bmatrix} \mathbf{x}(t) \\ \mathbf{z}(t) \end{bmatrix}^\top \begin{bmatrix} \mathbf{Q}_x & 0 \\ 0 & \mathbf{Q}_z \end{bmatrix} \begin{bmatrix} \mathbf{x}(t) \\ \mathbf{z}(t) \end{bmatrix} + \mathbf{u}(t)^\top \mathbf{R} \mathbf{u}(t) \right) dt,\tag{78}$$

where \mathbf{Q}_x is the state weighting matrix, \mathbf{Q}_z is the integral state weighting matrix, and \mathbf{R} is the control effort weighting matrix. The optimal control input is:

$$\mathbf{u}(t) = -\mathbf{K} \begin{bmatrix} \mathbf{x}(t) \\ \mathbf{z}(t) \end{bmatrix},\tag{79}$$

where \mathbf{K} is the feedback gain matrix obtained from solving the Algebraic Riccati Equation (ARE) for the augmented system.

The feedback gain \mathbf{K} is partitioned as:

$$\mathbf{K} = [\mathbf{K}_x \quad \mathbf{K}_z],\tag{80}$$

where \mathbf{K}_x corresponds to the state feedback, and \mathbf{K}_z corresponds to the integral action.

Design As for the LQR, the \mathbf{Q} and the \mathbf{R} matrices have been estimated in order to implement the LQI controller. The weighting parameters are the same except for the additional contribution which characterizes a huge relevance on the tracking error.

$$\mathbf{Q} = \begin{bmatrix} 25e^3 & 0 & 0 & 0 \\ 0 & 0 & 0 & 0 \\ 0 & 0 & 16e^{-2} & 0 \\ 0 & 0 & 0 & 10^6 \end{bmatrix}, \quad \mathbf{R} = 0.5.\tag{81}$$

The feedback gain matrix \mathbf{K} is thus been computed:

$$\mathbf{K} = [-513.31 \quad -9.19 \quad 1.71 \quad 4472.13].\tag{82}$$

Finally, the following eigenvalues have been computed to ensure control stability:

$$eig(\mathbf{A} - \mathbf{B}\mathbf{K}) = \begin{bmatrix} -19.74 + 0i \\ -46.54 + 53.49i \\ -46.54 - 53.49i \\ -92.40 + 0i \end{bmatrix}.\tag{83}$$

Step Response The measured data are reported in Figure 21 to exhibit the behavior of the system state correspondent to the application of a step signal.

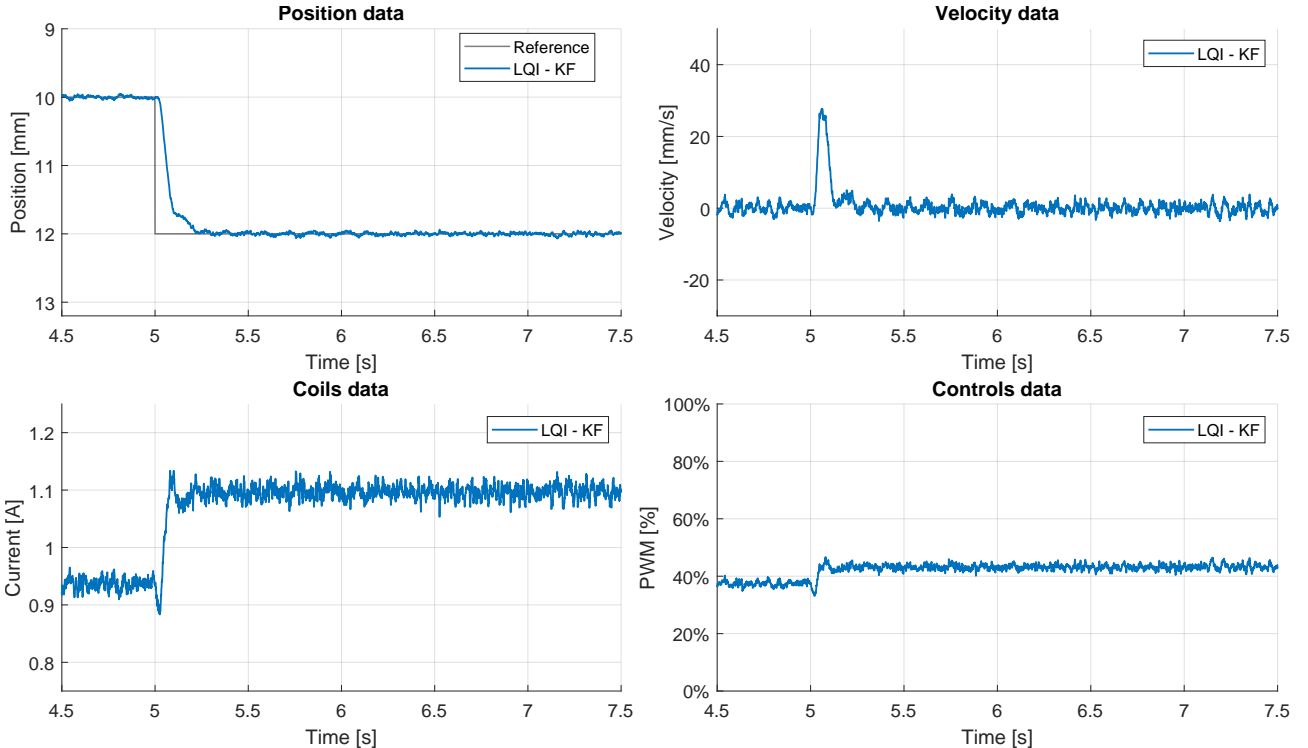


Figure 21: Step Response

7.3 MPC Controllers

Model Predictive Control (MPC) is an advanced control strategy widely used in industrial and engineering applications. It involves an optimization procedure which is continuously reinitialized as time goes on. This continuous adaptation of the control strategy makes the model very flexible and efficient in various applications. There exist many versions of MPC but, given the limited computational resources available, we have chosen to implement the linear MPC with constraints on the output variable. This version of MPC is based on a linear model of the system and is computationally less expensive than the nonlinear version.

The system is typically represented in discrete time as:

$$\begin{aligned} \mathbf{x}_{k+1} &= \mathbf{Ax}_k + \mathbf{Bu}_k \\ \mathbf{y}_k &= \mathbf{Cx}_k \end{aligned} \quad (84)$$

where x_k is the state vector at time k , \mathbf{u}_k is the control input at time k , \mathbf{y}_k is the output vector at time k , and $(\mathbf{A}, \mathbf{B}, \mathbf{C})$ are the system matrices.

At each time step k , the MPC controller solves an optimization problem such that the best control strategy is computed over the predefined time horizon, in order to get the state to the desired objective. Once the control action is applied, the system goes forward in time, and the optimization is reinitialized basing on the current state.

The optimization problem typically aims to minimize the objective function reported above, where the trade-off between tracking error and control effort over a finite prediction horizon N is researched:

$$\mathcal{J} = \sum_{k=0}^{N-1} [(\mathbf{x}_{k+1} - \mathbf{x}_{\text{ref}})^T \mathbf{Q} (\mathbf{x}_{k+1} - \mathbf{x}_{\text{ref}}) + \mathbf{u}_k^T \mathbf{R} \mathbf{u}_k], \quad (85)$$

where \mathbf{x}_{ref} is the reference trajectory, \mathbf{Q} is the weighting matrix for tracking error, and \mathbf{R} is the weighting matrix for control effort.

At each time step k , MPC solves the optimization problem:

$$\min_{\mathbf{u}_k, \dots, \mathbf{u}_{k+N-1}} \mathcal{J} \quad (86)$$

subject to:

$$\mathbf{x}_{k+i+1} = \mathbf{Ax}_{k+i} + \mathbf{Bu}_{k+i}, \quad i = 0, \dots, N-1. \quad (87)$$

Only the first control input \mathbf{u}_k is applied to the system, and the process is repeated at the next step. Since the optimization is done continuously and at each time step, the controller is robust so that if the system starts to deviate or the dynamics change over time we can modify the control behavior.

MPC is an attractive approach also because constraints can be imposed on the state or on the input. Indeed, the actuator physically has a saturation limit which cannot be overcome. Another advantage is that this control strategy works for nonlinear systems.

Since the initialization is repeated at each time step, fast hardware are necessary.

Design This efficient control strategy has also been implemented. Shorter prediction horizon has been selected to reduce computational effort.

$$\begin{aligned} \text{Prediction Horizon} &= 0.1s \\ \text{Control Horizon} &= 0.01s \end{aligned} \quad (88)$$

Constraints on the position and on the control are applied:

Variable	Max	Min
Position	20 mm	0 mm
Control	1	0

Table 7: Constraints for the MPC controller

Step Response The system response to an applied step signal is reported in Figure below.

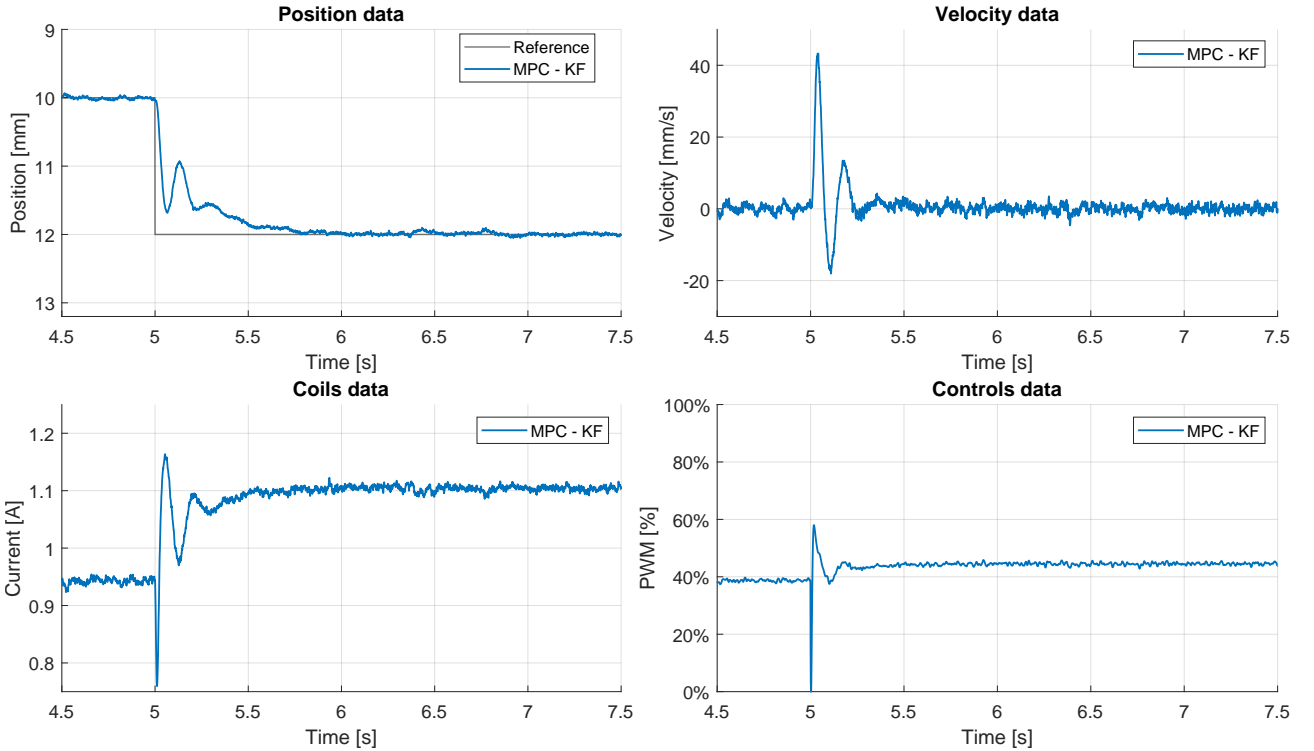


Figure 22: Step Response (MPC)

8 Results

To thoroughly assess the performance of the controllers and estimators & filters, several reference signals were designed to evaluate different aspects of system dynamics, including transient response, steady-state behavior, adaptability, and robustness.

In the following sections, we propose:

- **Controllers comparison:** a comparison between PIDs, LQs and MPC controllers as designed in Section 7. Results are obtained using Kalman filters to estimate and/or filter the system's state.
- **Filters comparison:** a comparison between the filters designed in Section 6. Results are obtained using an LQR tracking controller to evaluate the observer's ability to track the system's state during continuous oscillatory motion.

8.1 Controllers comparison

In the following sections, controllers designed in Section 7 are compared using different reference inputs signals. As stated in the introduction, all the results here presented are obtained using a Kalman filter to estimate and/or filter the system's state.

8.1.1 Multi-steps reference

A sequence of equally spaced step inputs is designed to assess the controller's response to abrupt set-point changes and its steady-state performance across various set-points.

Two versions of the multi-steps reference signals are explored:

- **Up & down:** signal designed to evaluate the controller's performance by moving the sphere in both directions relative to the linearization point, using steps of amplitude 2[mm]. This test assesses the controller's ability to maintain stability and accuracy during repeated set-point changes, as well as its robustness in handling deviations in both directions.
- **Stairs:** signal with steps always in the same direction, ranging from 8[mm] to 12[mm] with a resolution of 1[mm]. This test is particularly useful for analyzing the controller's response to minor perturbations and its capacity for gradual positional adjustments.

The following figures show the comparison of the controllers using the multi-steps reference signals.

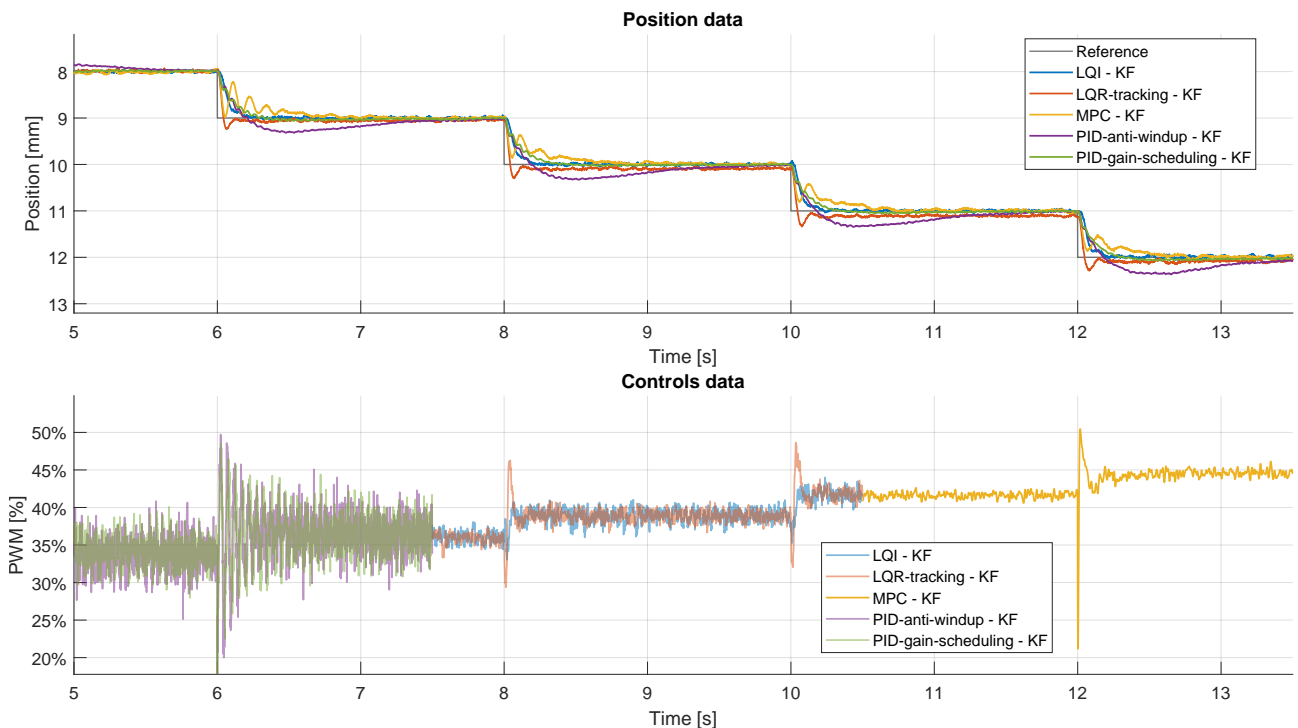


Figure 23: Comparison of controllers with multistep stairs reference using KF

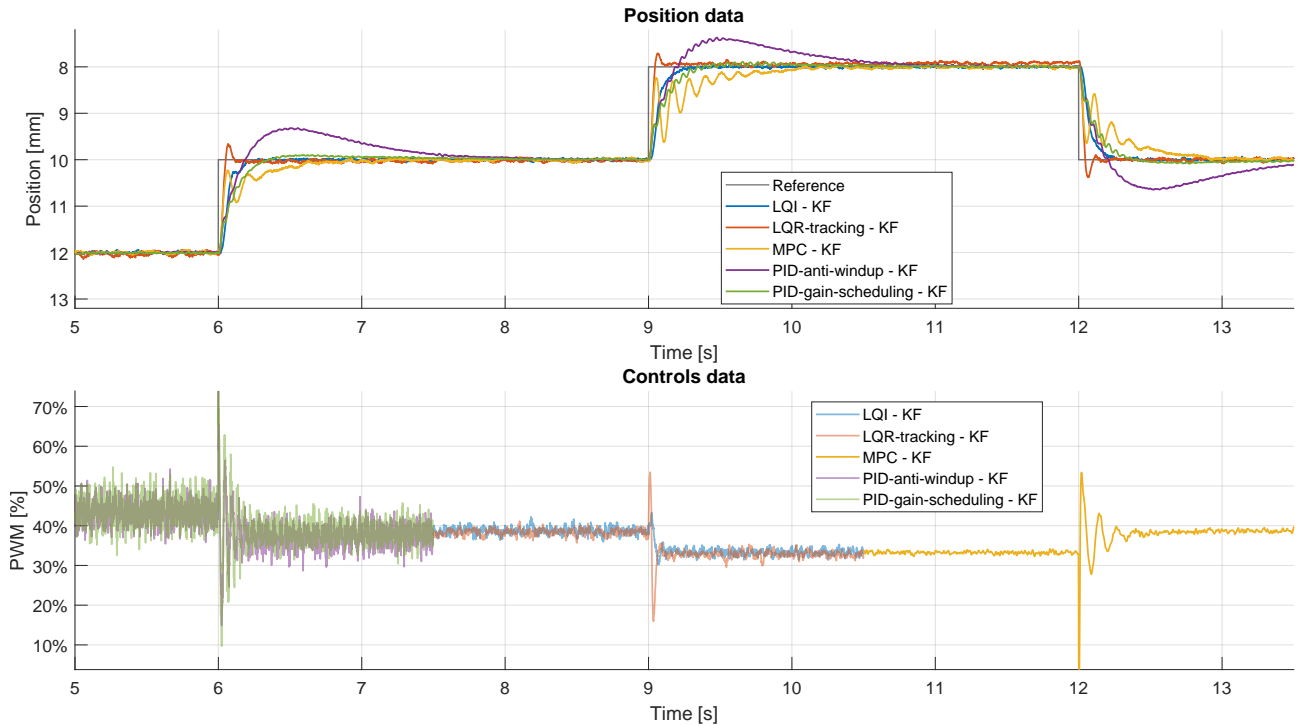


Figure 24: Comparison of controllers with multistep up & down reference using KF

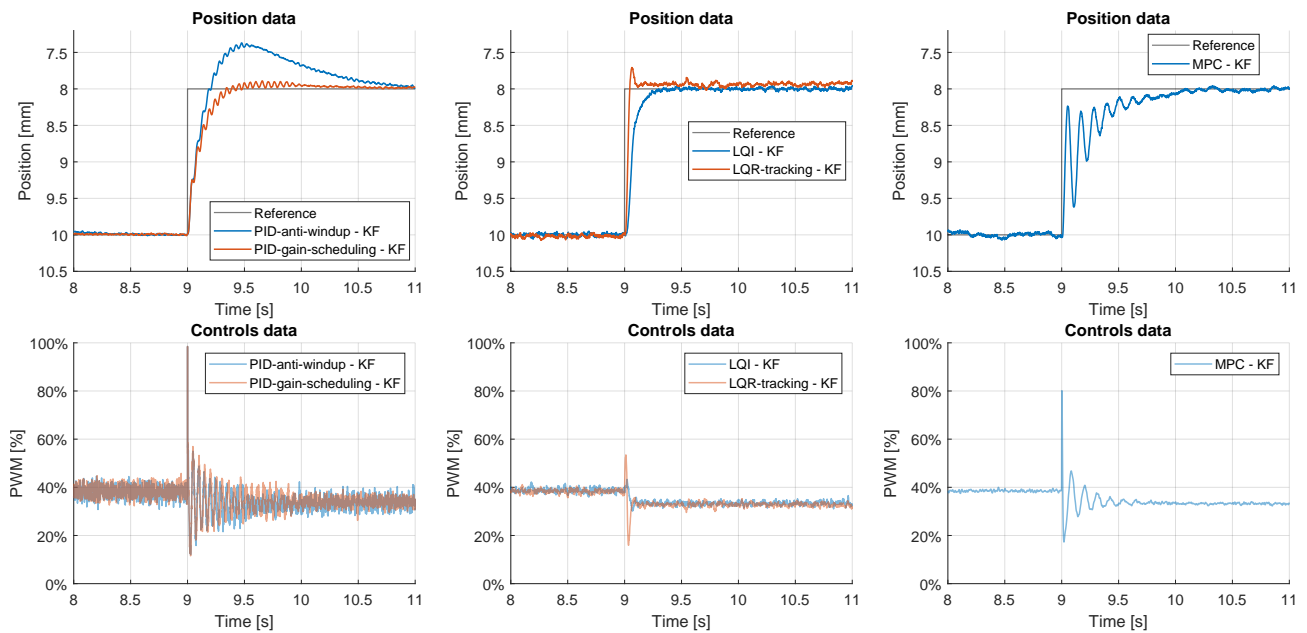


Figure 25: PIDs, LQs, MPC with multistep up reference using KF

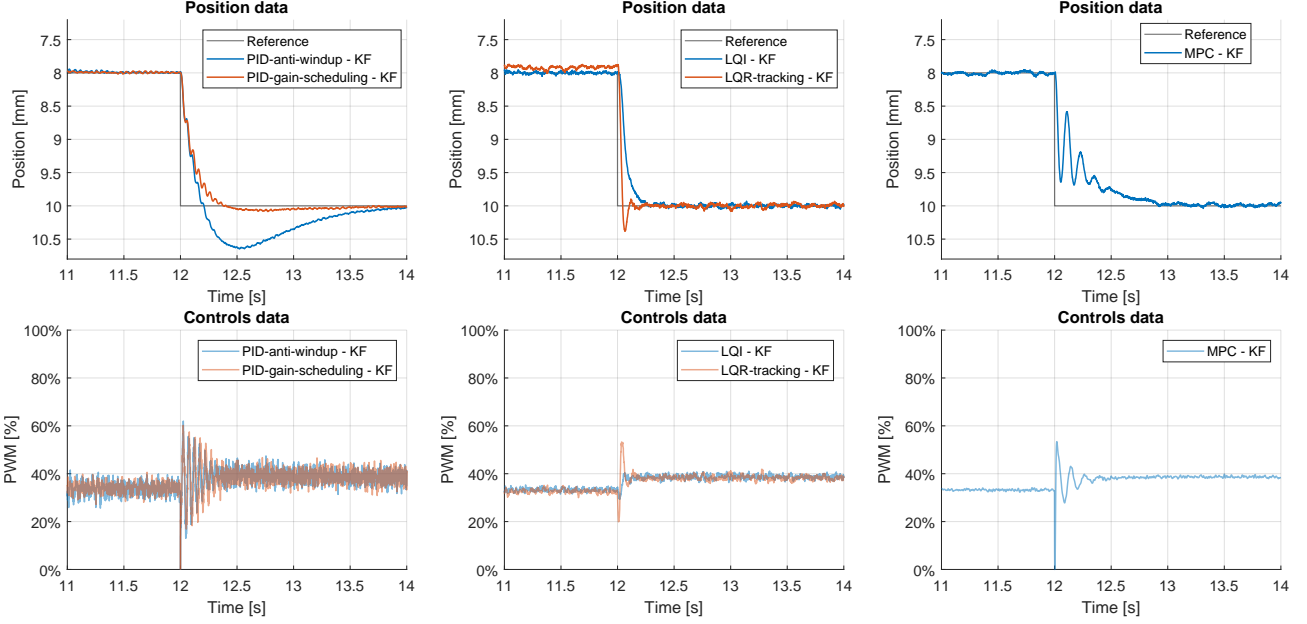


Figure 26: PIDs, LQs, MPC with multistep up & down (down) reference using KF

PID anti-windup The PID anti-windup controller exhibits the response that deviates the most from the reference data compared to the other developed controllers.

The trajectory presents an overshoot before the sphere approaches the correct value. This behavior clearly delays the achievement of the reference position. In fact the sphere reaches the reference position just in time before it is changed.

The control exhibits numerous oscillations and peaks, particularly during transitions.

The slowness in approaching the target position makes the PID anti-windup unsuitable for rapid reference changes.

PID gain scheduling According to the theory, the performance of the PID, is significantly enhanced by the development of PID gain scheduling.

Using multiple linearization, it enables a much more accurate trajectory of the sphere, free from overshoots and considerably faster.

Additionally, the control behavior in the case of PID gain scheduling is cleaner respect to the anti-windup case, but not respect to the other controllers.

The effectiveness of PID gain scheduling is limited by the linearity of the model: in the presence of non-linearities or complex dynamics, it cannot compete with advanced techniques such as LQR or LQI.

LQR tracking The LQR tracking controller exhibits reduced error during the transient phase, with small oscillations as the set points are reached. In steady state, the error is small, but the accuracy can be enhanced by the use of LQI controller. A small overshoot peak is observed prior to stabilization.

Dynamically, the response is very fast, demonstrating that LQR tracking is the quickest controller among those implemented.

The control behavior is highly smooth and significantly outperforms both the PID anti-windup and the PID gain scheduling. The control signal presents some peaks during the steps, but they remain well-contained.

The small oscillations observed are due to the lack of an integral component, which does not allow to completely cancel constant errors.

LQI The LQI controller, leveraging its integral term, compensates the accumulated error over time. In steady state, the sphere approaches the reference trajectory with smaller discrepancy compared to the LQR tracking case.

Dynamically, the transitions are less aggressive, and the overshoot is reduced, at the cost of a slightly increased stabilization time.

The control exhibits small fluctuations and avoids the peaks observed in the tracking case. The LQI control establishes itself as the cleanest control signal, as demonstrated in all the figures above.

The slower stabilization is a consequence of the more controlled and less aggressive dynamics compared to LQR. Compared to the LQR, the LQI is particularly suitable for applications where stability and accuracy are more important than response speed.

MPC The MPC exhibits a more oscillatory behavior compared to LQR or LQI, with pronounced oscillations during set point transitions. These oscillations are particularly noticeable at reference step changes. In steady-state conditions, the MPC sufficiently reduces the error, stabilizing more slowly than LQI and PID gain scheduling, but faster than the PID anti-windup. The MPC is more aggressive in attempting to reach the set point. The control graph shows oscillations and peaks during position changes, which remain contained. The MPC control is less smooth than LQI and LQR tracking but is better respect both the PID controllers. MPC is best suited for complex, multivariable scenarios, but in cases with rapid transitions it may be less smooth than LQR and LQI.

8.1.2 Sinusoidal (discrete) reference

As a second reference signal for the comparison of the controllers, we propose the sinusoidal (discrete) reference. Here the input signal is a sinusoidal shape, but represented as a sequence of discrete steps. The period on the sinusoidal is 2 seconds, and the amplitude is 2[mm] centered around 10[mm].

The following figures show the comparison of the controllers using the sinusoidal reference signals.

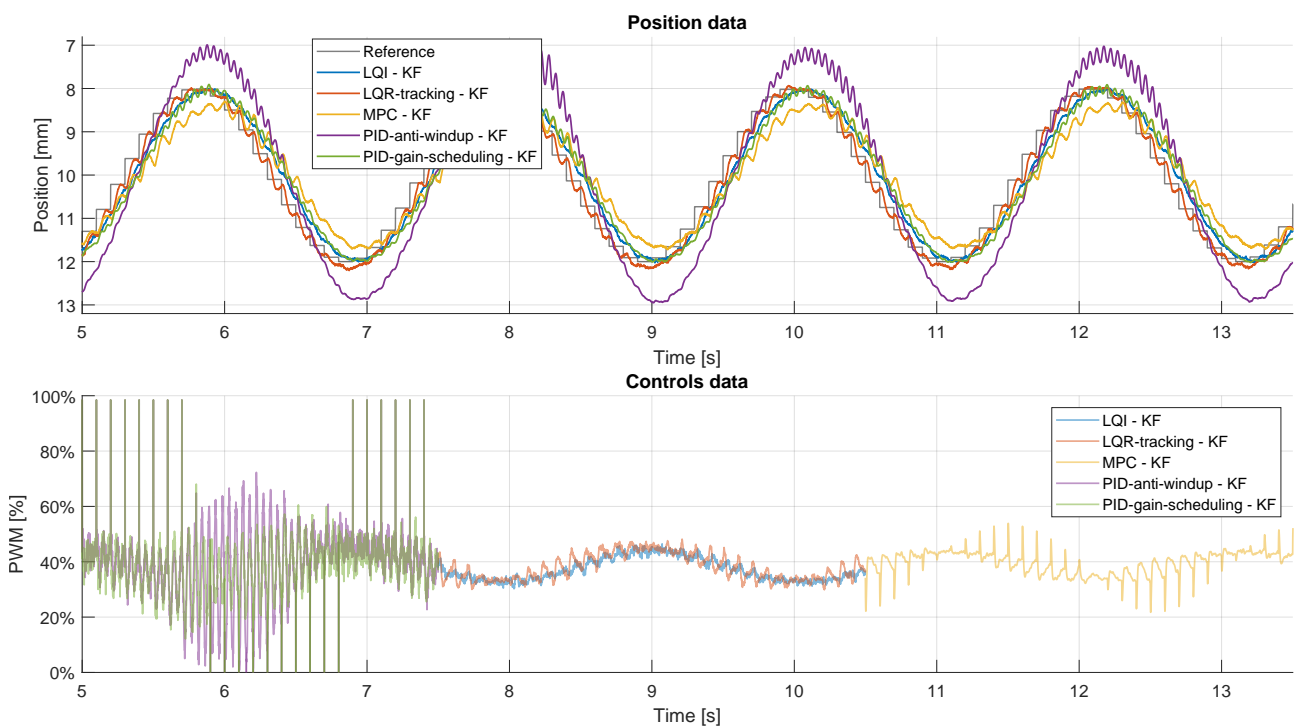


Figure 27: Comparison of controllers with sinusoidal fast reference using KF

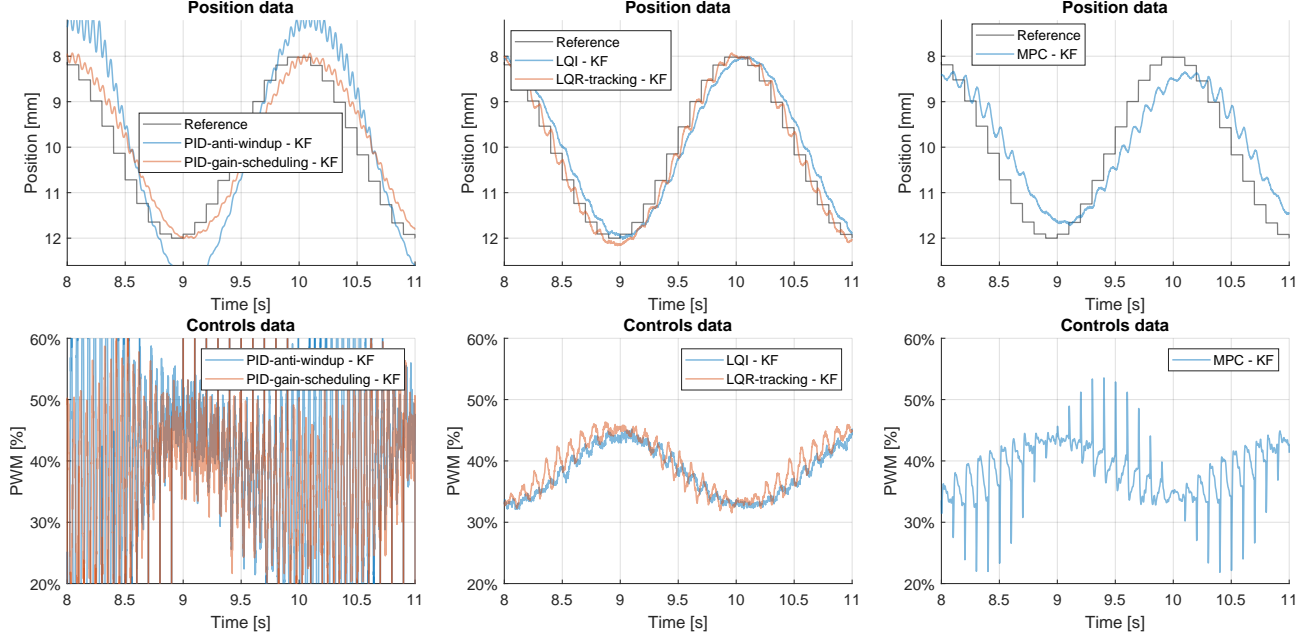


Figure 28: PIDs, LQs, MPC with sinusoidal fast reference using KF

PID anti-windup As with the multistep reference, in the case of the fast sine reference, the PID anti-windup controller proves to be the least effective.

The nature of the PID and the inability to anticipate dynamics make it difficult to manage a rapidly varying trajectory such as a stepped sine. It deviates from the desired trajectory much more significantly compared to the other controllers developed and exhibits greater oscillations, particularly when the sphere is closer to the upper coil.

The control performance is also the worst when compared to the other controllers, with large oscillations at the extreme points of the sine wave.

PID gain scheduling The PID gain scheduling significantly reduces oscillations of the trajectory, as observed in the multistep reference, demonstrating a much better performance than the anti-windup case. However, it still shows oscillations, particularly when the sphere reaches a distance of 8 mm from the upper coil.

The control remains really inadequate with large oscillations, in particular at the extreme points of the sinusoidal.

LQR tracking The LQR tracking is highly accurate, with the trajectory closely following the reference and exhibiting small oscillations. The control is much improved, without saturation and very low oscillations.

LQI The LQI, thanks to its integral term, is able to follow the reference even more precisely than the LQR tracking. It once again proves to be the best controller for achieving an accurate and fast response with very clean control.

The control signal is smooth, without peaks or large oscillations. The fast sine reference demonstrates the great performance of this controller. The LQI is able to manage not only the dynamic trajectory, but also to maintain a practically zero error at steady state, proving to be the cleanest and most stable.

MPC Despite some trajectory delay due to prediction calculations, the MPC is able to follow the reference, proving to be a sufficient controller even for a fast dynamic system like this one.

The control exhibits several peaks, but they are always well contained. As it was written for the multistep case, MPC is best suited for complex, multivariable scenarios, but in this case the performance is inferior respect to LQR tracking and LQI.

8.1.3 Conclusions

The comparative analysis of the controllers reveals significant differences in performance across various scenarios. The PID anti-windup controller is the least effective, exhibiting slow and oscillatory behavior with a noticeable delay in reaching the reference position. It struggles to maintain trajectory adherence and minimize oscillations, particularly at smaller distances from the upper coil.

The PID gain scheduling improves performance compared to the PID anti-windup by reducing overshoot and increasing response speed. However, it still suffers from large oscillations and peaks in the control signal, making it unsuitable for this system.

The LQR tracking controller provides faster responses with minimal error and exhibits a clean control signal, making it an effective solution for precise and rapid adjustments.

The LQI controller offers the best performance overall, combining stability, accuracy, and clean control. It achieves a more stable response with fewer oscillations compared to the LQR and other controllers, making it the most consistent and reliable choice for this study.

The MPC controller, while more aggressive, demonstrates adequate tracking of the reference. However, it introduces oscillations during reference changes, resulting in less smooth control compared to other methods. Additionally, its performance is hindered by delays from prediction calculations, highlighting the need for further tuning and optimization.

In summary, the LQI controller stands out as the optimal solution for precise, rapid, and smooth control, delivering the most consistent performance across all tests.

8.2 Filters and Estimators comparison

In this section, we compare the filters and estimators designed in Section 6, using an LQR tracking controller to assess their ability to track the system's state during continuous oscillatory motion.

The primary objective is to evaluate the effectiveness of each filtering method in ensuring accurate tracking of the sphere's trajectory relative to the sinusoidal reference, as well as the quality of the resulting control signal. To achieve this, a continuous sinusoidal reference signal with a period of 6 seconds is used. This setup allows us to analyze the filters' performance in handling gradual oscillations. As in the sinusoidal input used for the controllers comparison, the oscillations range between 12[mm] and 8[mm].

The following figures illustrate the performance of the filters and estimators in tracking the system's state under these oscillatory conditions.

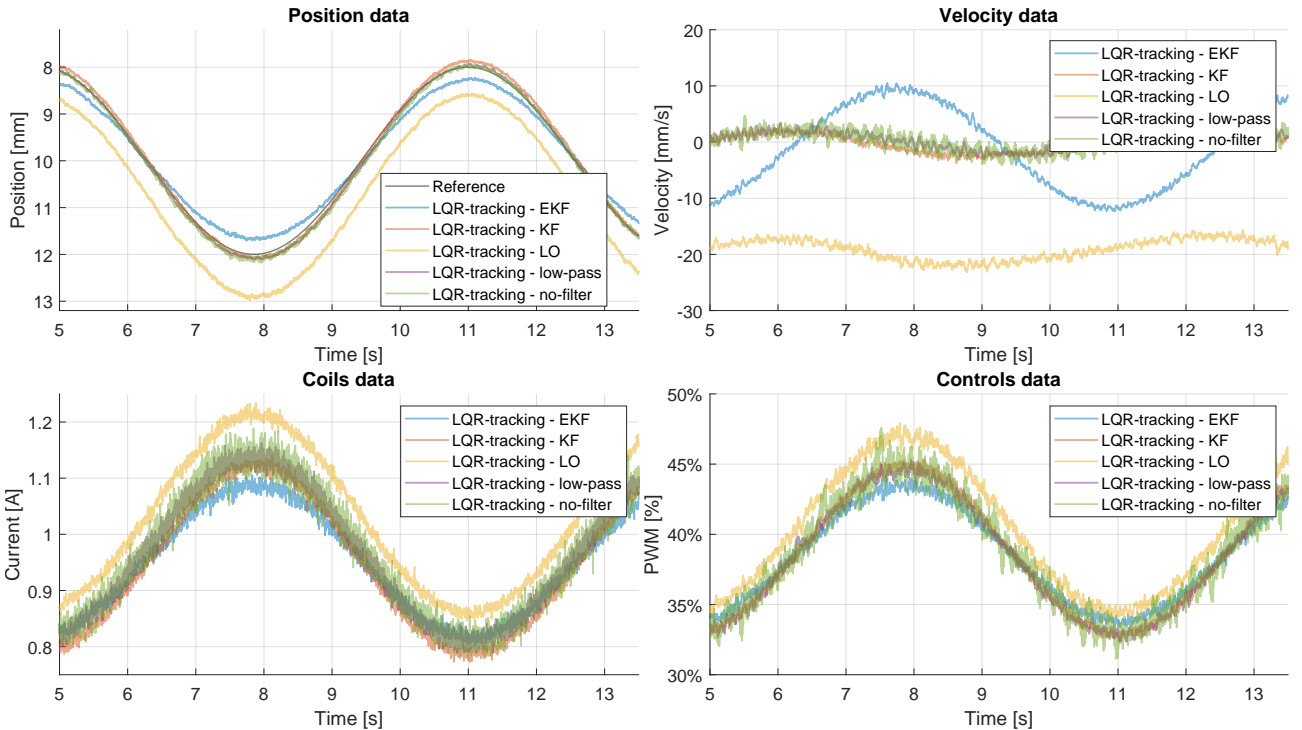


Figure 29: Comparison of filter using an LQR tracking with sinusoidal slow reference

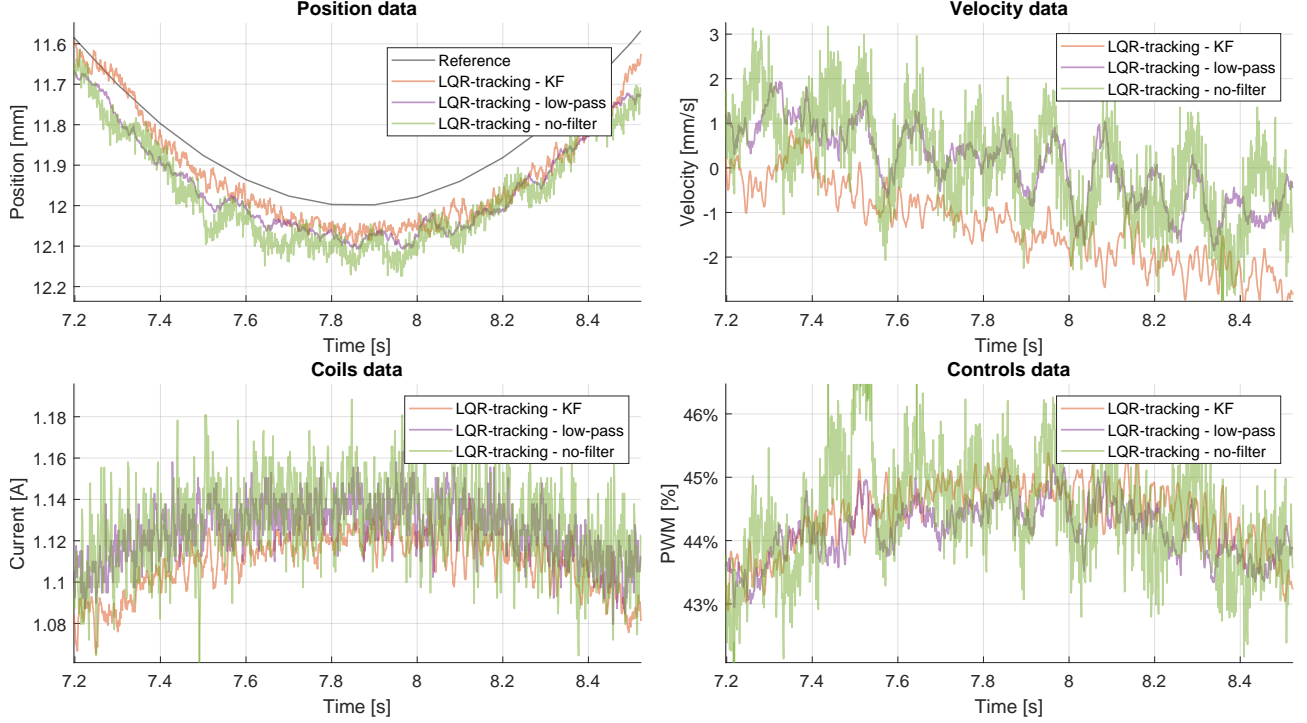


Figure 30: Comparison of no filter, low pass, KF using an LQR tracking with sinusoidal slow reference

Raw measurements Clearly due to the absence of filtering, the system noise is not reduced. Noise filtering, especially for velocity, is critical to achieving accurate response. Using the controller without filters results in the least precise trajectory tracking.

The control performance is visibly affected by oscillations, making this approach not optimal for the system under consideration.

Low pass filter Introducing a low pass filter improves the response accuracy compared to the unfiltered case. However, its ability to eliminate noise is limited by the filter's non-adaptive nature, which hinders dynamic performance. The accuracy is higher respect to the case without filters, but lower respect to the other filters except for the Luenberger observer.

Luenberger observer (LO) This case represents the least effective way to estimate the state.

The Luenberger observer can be worse than the unfiltered case because it uses a non-optimal fixed-gain feedback, amplifying the noise and introducing errors in the state estimation. Furthermore, by not handling stochastic noise statistically, it compromises the control, which in this case is less precise than using the noisy measurements directly.

Standard Kalman filter (KF) The Kalman filter emerged as the most effective method among those tested. Its ability to optimize state estimation in the presence of measurement and process noise significantly enhances control quality. As a consequence, the control signal is more accurate and less noisy, leading to improved system performance. The trajectory tracking exhibited the highest accuracy with minimal oscillations.

Extended Kalman filter (EKF) Although the EKF is designed to handle system non-linearities, the results showed inferior performance compared to the standard Kalman filter. Specifically, the EKF failed to adequately follow the reference trajectories.

This could be attributed to suboptimal linearizations or poorly tuned covariance matrices. These findings suggest that applying the EKF requires further investigation and optimization to achieve competitive performance.

8.2.1 Conclusions

The comparative analysis highlighted a clear hierarchy in the performance of the various approaches.

The standard Kalman filter stands out as the optimal solution for the analyzed system, ensuring precise and stable control. In contrast, the Luenberger observer is the least effective way to filter. Despite its theoretical potential, the EKF delivered unsatisfactory results compared to its simpler counterpart, indicating that further tuning is required.

9 Conclusions

In this study, we have presented the modeling and control strategies for a Magnetic Levitation System (MLS), which represents an intriguing and highly challenging application of control theory. The MLS system is characterized by highly nonlinear dynamics and unstable equilibrium conditions, making it a suitable test bed for advanced control techniques. The system consists of two electromagnets, a ferromagnetic sphere, and a control unit, with the primary objective being the levitation of the sphere at a precise height by regulating the current in the electromagnets.

Initially, a comprehensive model of the system was derived, capturing the key dynamics involved in the interaction between the electromagnets and the sphere. After deriving the model, the system parameters were identified, and various filtering and estimation techniques were implemented to estimate the state of the system based on available input and output signals. The filters employed in this study included the Luenberger observer, a low-pass filter, the standard Kalman filter (KF), and the Extended Kalman filter (EKF). Through a thorough comparative analysis of these filtering methods, it was determined that the standard Kalman filter offered the most efficient performance. The Kalman filter excelled in noise reduction, particularly in the velocity signal, which is critical for achieving precise trajectory tracking and ensuring the accuracy and quality of the control signal. The reduction in noise not only enhanced the overall performance of the system's output but also ensured smoother and more reliable control actions.

Once the filtering techniques were implemented, several control strategies were developed and tested to regulate the position of the levitating ball, with the overarching goal of ensuring both precise and stable control. The controllers that were evaluated include the PID controller with anti-windup, the PID controller with gain scheduling, Linear Quadratic Regulator (LQR) tracking, Linear Quadratic Integral (LQI) control, and Model Predictive Control (MPC). The performance of each of these controllers was assessed in terms of their ability to stabilize the system and enable accurate tracking of the desired position of the levitating ball. The results demonstrated that all the controllers are able to control the sphere, although they exhibited varying levels of performance.

Among the tested controllers, the LQI controller emerged as the most effective. The LQI controller not only achieved accurate control of the ball's position but also provided a clean control signal with minimal oscillations and overshoot, contributing to the overall robustness and reliability of the system. This characteristic is particularly important for ensuring smooth and efficient operation, avoiding undesirable system behavior such as excessive vibrations or instability.

The successful modeling, estimation, and control of the Magnetic Levitation System in this study demonstrate the effectiveness of the proposed approach and the various controllers tested. The results are promising, offering a solid foundation for further exploration and refinement of the techniques employed. Future research could focus on the development of even more advanced control strategies, such as Feedback Linearization or Backstepping controllers, which have the potential to further enhance the performance of the system, especially under more dynamic and challenging conditions. These advanced techniques could provide additional benefits, such as improved system robustness and adaptability, and might offer better performance in handling larger disturbances, non-linearities, and uncertainties.

References

- [1] Shencheng Ge, Alex Nemiroski, Katherine A. Mirica, Charles R. Mace, Jonathan W. Hennek, Ashok A. Kumar, and George M. Whitesides. Magnetic levitation in chemistry, materials science, and biochemistry. *Angewandte Chemie International Edition*, 59(41):17810–17855, 2020.
- [2] INTECO. Magnetic levitation systems — inteco. <https://www.inteco.com.pl/products/magnetic-levitation-systems/>, 2014. [Online; accessed 26-September-2024].
- [3] Marcin Jastrzebski and Jacek Kabzinski. Adaptive control of magnetic levitation system based on fuzzy inversion. *Scientific Reports*, 14(1):24815, Oct 2024.
- [4] Federico Ongaro, Stefano Pane, Stefano Scheggi, and Sarthak Misra. Design of an electromagnetic setup for independent three-dimensional control of pairs of identical and nonidentical microrobots. *IEEE transactions on robotics*, 35(1):174–183, February 2019.
- [5] Hamid Sanavandi and Wei Guo. A magnetic levitation based low-gravity simulator with an unprecedented large functional volume. *npj Microgravity*, 7(1):40, Oct 2021.
- [6] Wikipedia contributors. Scmaglev — Wikipedia, the free encyclopedia. <https://en.wikipedia.org/w/index.php?title=SCMaglev&oldid=1243224393>, 2024. [Online; accessed 28-September-2024].
- [7] Tiantian Xu, Jiangfan Yu, Xiaohui Yan, Hongsoo Choi, and Li Zhang. Magnetic actuation based motion control for microrobots: An overview. *Micromachines*, 6(9):1346–1364, 2015.